

Control of Laminar Boundary Layers using Electro Active Polymers

by

Tyler Van Buren

A Thesis Submitted to the Graduate
Faculty of Rensselaer Polytechnic Institute
in Partial Fulfillment of the
Requirements for the degree of
MASTER OF SCIENCE
Major Subject: Aeronautical Engineering

Approved:

Michael Amitay, Thesis Adviser

Rensselaer Polytechnic Institute
Troy, New York

July, 2010
(For Graduation August 2010)

CONTENTS

Control of Laminar Boundary Layers using Electro Active Polymers.....	i
LIST OF FIGURES	iv
ACKNOWLEDGMENT	vi
ABSTRACT	vii
1. INTRODUCTION	1
1.1 Motivation.....	1
1.1.1 Micro Air Vehicle Flight.....	1
1.1.2 Boundary Layer Instabilities	3
1.1.3 Mixing Layer Instabilities	4
1.1.4 Laminar Separation Bubbles	9
1.1.5 Flow Control of Laminar Boundary Layers.....	9
2. EXPERIMENTAL SETUP	11
2.1 Wind Tunnel Restoration	11
2.1.1 Inlet	11
2.1.2 Test Section.....	12
2.1.3 Outlet.....	12
2.2 FLAT PLATE DESIGN.....	16
2.2.1 Flat Plate	16
2.2.2 Leading Edge	16
2.2.3 Flap.....	16
2.2.4 EAP Plugs	17
2.2.5 EAP Devices	17
3. RESULTS	24
3.1 EAP CALIBRATION	24
3.2 BOUNDARY LAYER MEASUREMENTS	33
3.2.1 Experimental Procedure.....	33

3.2.1.1 Hot-wire Calibration	34
3.2.1.1 Boundary Layer Experimental Procedure	35
3.2.2 Results and Discussion.....	35
4. CONCLUSION.....	56
4.1 EAP Calibration	56
4.2 Boundary Layer Measurements	56
5. RECCOMENDATIONS FOR FUTURE WORK.....	58
Bibliography	59

LIST OF FIGURES

Figure 1.1 - Artistic representation of a low Reynolds number flow field over an airfoil (Bastedo and Mueller, 1986)	5
Figure 1.2 - Representation of an Electro-Active Polymer implementation on a MAV. ..	6
Figure 1.3 - Curves of neutral stability for 2D boundary layer for the (a) non-viscous instability and (b) for viscous instability (Schlichting, 1979, pg. 461)	7
Figure 1.4 - Growth rate as a function of wavenumber for a laminar mixing layer profile. (Criminale et al., 2003, pg. 67).....	8
Figure 2.1 - Wind tunnel schematic.....	14
Figure 2.2 - Test section	15
Figure 2.3 - CAD model of the flap plate design. Dark grey represents aluminum, light grey represents SLA	19
Figure 2.4 - Fabricated flat plate.....	20
Figure 2.5 - Trailing edge flap and its mechanism	21
Figure 2.6 - EAP layer configuration, CAD representation	22
Figure 2.7 - EAP hole configuration.....	23
Figure 3.1 - EAPs surface: (A) unactuated, and (B) actuated	27
Figure 3.2 - Time varying of the EAP surface velocity; driving frequency is 50 Hz and input voltage of 2,000V	28
Figure 3.3 - LDV setup for the EAP calibration experiments	29
Figure 3.4 - Streamwise variation of the EAP displacement; driving frequency 50Hz and 150Hz, input voltage 1000V and 2,000V	30
Figure 3.5 - 3D surface deflection at 40Hz and 2000V.....	31
Figure 3.6 - 3D surface deflection at 500Hz and 2000V	32
Figure 3.7 – View of the hotwire probe in the test section equipped with the flat plate .	40
Figure 3.8 - Close up view of the hot-wire in the wind tunnel, EAP installed.....	41
Figure 3.9 - Boundary layer comparison to the Blasius solution, streamwise location 6.5”, flap angle 0°	42
Figure 3.10 - Boundary layer comparison to the Falkner-Skan solution for $\beta = -0.05$, streamwise location 6.5”, flap angle 12°	43

Figure 3.11 - Normalized boundary layer profiles offset by their streamwise location from the plate leading edge for two flap deflections: 0° and 12°	44
Figure 3.12 - Boundary layer evolution, flap angle 12° , normalized velocity offset by streamwise location from the leading edge, 95% U_∞ line included.....	45
Figure 3.13 - Normalized boundary layer profiles offset by different plate locations, with and without EAP installed and un-actuated.....	46
Figure 3.14 - Normalized boundary layer profiles, baseline (unactuated), different streamwise locations (A) 7.5", (B) 8.0", (C) 8.5", (D) 9.0", (E) 9.5", (F) 10.0", and (G) 12.0".....	47
Figure 3.15 - Turbulence intensity profiles, baseline (unactuated), different streamwise locations (A) 7.5", (B) 8.0", (C) 8.5", (D) 9.0", (E) 9.5", (F) 10.0", and (G) 12.0".....	48
Figure 3.16 - Normalized boundary layer profiles, actuation frequency = 40 Hz, different streamwise locations (A) 7.5", (B) 8.0", (C) 8.5", (D) 9.0", (E) 9.5", (F) 10.0", and (G) 12.0".....	49
Figure 3.17 - Turbulence intensity profiles, actuation frequency = 40 Hz, different streamwise locations (A) 7.5", (B) 8.0", (C) 8.5", (D) 9.0", (E) 9.5", (F) 10.0", and (G) 12.0".....	50
Figure 3.18 - Normalized boundary layer profiles, actuation frequency = 500 Hz, different streamwise locations (A) 7.5", (B) 8.0", (C) 8.5", (D) 9.0", (E) 9.5", (F) 10.0", and (G) 12.0".....	51
Figure 3.19 - Turbulence intensity profiles, actuation frequency = 500 Hz, different streamwise locations (A) 7.5", (B) 8.0", (C) 8.5", (D) 9.0", (E) 9.5", (F) 10.0", and (G) 12.0".....	52
Figure 3.20 - Normalized boundary layer profile and turbulence intensity for different actuation frequencies, distance from leading edge = 8.0".....	53
Figure 3.21 - Normalized boundary layer profile and turbulence intensity for different actuation frequencies, distance from leading edge = 9.5".....	54
Figure 3.22 - Normalized boundary layer profile and turbulence intensity for different actuation frequencies, distance from leading edge = 12.0".....	55

ACKNOWLEDGMENT

I would like to thank Dr. Michael Amitay for his wisdom and insight when advising the project. I would like to express my gratitude to Dave Digiulio for providing invaluable teachings with all the machining done. I would also like to thank the valued members of my research laboratory for the advice given throughout the project, especially John Vaccaro who was the hero to the project numerous times. Lastly I would like to thank Jeff Beckford, my friend and undergraduate assistant, for the late nights to early mornings working with me in the lab when we should have been home sleeping.

ABSTRACT

Micro air vehicles (MAV) are a major focus of aerodynamics today with many military as well as civilian applications. MAV flight instability is dominated by the unsteady characteristics of low Reynolds number flows. Three dimensional separations occur at random on different parts of the wing due to gust causing highly unsteady lift conditions as well as full wing stall. An Electro-Active Polymer (EAP) was examined in this work as a flow control device with application to MAVs.

Laser Displacement experiments were conducted to calibrate the EAP and examine the displacements generated under selected frequencies and voltages. It was shown that the deflections could reach up to 0.35mm at high frequencies (40Hz). The surface deflection was found to be parabolic across the span and width of the actuator.

Hot-wire measurements were conducted on a flat plate equipped with a trailing edge flap in a low Reynolds number wind tunnel to study the effects of the EAP on the boundary layer in the presence of an adverse pressure gradient. Two actuation frequencies, corresponding to the Tollmien-Schlichting waves of the boundary layer and the Kelvin-Helmholtz waves (due to the presence of an inflection point). The disturbance frequency corresponding to the inflection point was found to be the most effective in altering the boundary layer as well as the turbulence intensities.

1. INTRODUCTION

1.1 Motivation

1.1.1 Micro Air Vehicle Flight

At lower Reynolds numbers the flow is dominated by viscosity and thus more susceptible to separation. A micro air vehicle (MAV) can experience flow separation due to varying flow conditions such as gusts and turbulence that can induce laminar separation bubbles (LSB) on the wings (Figure 1.1 shows an artistic representation of 3D separation bubble over an airfoil at a low Reynolds number). Given that MAVs are a relatively new technology it is important to fully understand the flow field at this low range of Reynolds numbers and address this issue or separation bubble using advance active flow control technique, which the motivation of the present work.

Flow control has been a rising field in fluid dynamics over the last few decades with a wide variety of techniques in aerodynamics alone. In Gad-el-Hak's flow control book (2000) the author describes flow control to have been born with Prandtl's (1904) introduction of boundary layer theory, presenting the behaviors of boundary layers and flow separation as well as some experiments in which the boundary layer was controlled. Since then different eras have induced new methods of flow control, whether it be World War II and the Cold War's demands for better missiles, torpedoes, ships, and aircrafts, or the energy crisis that has developed since the 1970s that has shifted aerodynamic advancement interests to civilian transport. Laminar flow control, which refers to keeping flow laminar by delaying transition, has been a large advancement in improving aircraft flight. Joslin (1998) reviewed successful laminar flow control (LFC) techniques on aircrafts from the 1930's to the 1990's. Techniques of LFC range from wing shaping using flaps and leading edge mechanisms to suction on the wing surface, and even ways of removing roughness due to insect contamination. The author describes the benefits of LFC with an example: using LFC on the A340 over the first 15% of the chord resulted in a drag reduction of 14% on the wing, a very significant and cost saving advancement. Thibert et al. (1990) reports that roughly 50% of the total drag of a subsonic transport aircraft is caused by skin-friction drag and this significant portion of the drag can be reduced significantly if the flow were kept laminar due to the fact that laminar flow can

have 90% less skin friction than turbulent flows. Another portion of flow control comes from the reverse of LFC, the process of transitioning to turbulence earlier to prevent separations. Mueller et al (2003) reviewed the problems with MAV flight that must be addressed to advance the technology. A significant portion of problems with MAVs is contributed to laminar separation. At Reynolds numbers below 70,000 the author reports that when laminar separation occurs (often due to gusts) the flow does not transition fast enough for reattachment on the wing and thus causing full stall. For Reynolds numbers from 70,000-200,000, laminar separation often reattaches on the airfoil causing laminar separation bubbles, which can still pose problems to flight performance due to parasitic drag of the LSB and the unsteady lift associated with it. This motivates the need for an active flow control device that promotes earlier transition and thus reduces the negative effects of laminar separation.

Active flow control is defined as a technique which can be turned on and off as needed, unlike passive flow control in which the effects are always present on the flow field. Morphing surfaces have been a relatively new and exciting form of active flow control. The ability to change the shape of a surface has been shown to significantly affect flow fields on large scales. Pinkerton and Moses (1997) studied the feasibility of using a special high displacement piezoelectric actuator designed at NASA (THUNDER actuator) as a shape altering mechanism on a subscale airfoil. The goal of the research was to show that the actuator was successful in significantly changing the camber under multiple wind tunnel velocities, which was anticipated to extend the region of attached flow over the airfoil at angles of attack above 2 degrees. They found that actuation successfully altered the wing camber with multiple parameters effecting the actuator displacement: magnitude of the applied voltage, tunnel velocity, the angle of attack, and creep and hysteresis of the wafer.

Ehlers and Weisshaar (1993) studied the ability of piezoelectric actuators in changing lift characteristics of swept and unswept wings by changing the wings aeroelastic stiffness. Feedback control sensed wing root strains and adjusted active actuator layers to proportionally change wing lift. They found that although lift was successfully adjusted, the effectiveness of the actuator is strongly constrained by the stiffness of the piezo material as well as the implementation of the device on the wing.

Ifju et al. (2002) investigated the development of flexible-wing-based MAV technology to reduce the negative effects of gust conditions. They demonstrated flexible wing concepts on wingspans from 5” to 18” reporting the flexible wing design, fabrication methods, as well as flight data analysis. Through pilot reports and video recordings they reported much smoother flight conditions for a variety of test vehicles. They continue to conduct works to better quantify the advantages of flexible wing airfoils.

In recent years Electro Active Polymer (EAP) technology has been shown to be a simple solution to surface morphing. The technology not only provides means to static morphing with a constant DC voltage input, but also the means of dynamically adding disturbances to the flow for the purpose of promoting early transition. Figure 1.2 represents a possible implementation of EAP technologies on a MAV for either promote transition or maintain a laminar flow. Dearing et al. (2007) used EAPs as a means to produce an active dimple to induce controlled vorticity into the flow field. They analyzed the effect of a single actuated dimple with a flow field using PIV and flow visualizations. They reported that a smooth dimple generates vorticity in phase with the dimple motion and the strength of vorticity is in proportion to dimple displacement. Before using any flow control device, especially in an unsteady mode, it is first needed to explore the inherent instabilities in boundary layers and mixing layers to better implement the actuator (in the present work, the actuator is the EAP).

1.1.2 Boundary Layer Instabilities

Boundary layer instability is a subject that has been discussed for quite some time, and boundary layer transition has been a subject of study since the late 1800’s. Tollmien (1962) and Schlichting (1932) made the discovery of convective traveling wave instabilities, which have been rightly termed Tollmien-Schlichting (TS) waves. This is the dominant frequency that is the main source of transition to turbulence in most laminar flows. TS waves can be derived for particular flows relatively simply using the solution for a laminar boundary layer on a flat plate with zero pressure gradient, portrayed through the Blasius boundary layer solution. Using this boundary layer equation, and assuming small disturbances, yields the Orr-Sommerfeld equation from

which it is possible to derive the critical Reynolds number along with the most unstable modes for a given Reynolds number (for details see Schlichting's book,1979). Figure 1.3 portrays the neutral stability curves for different boundary layer instabilities. Gaster (1974) investigated the stability of traveling-wave disturbances over a flat plate. The neutral stability boundaries solutions are given and compared with experimental data. He concludes that the parallel flow assumption is valid at high Reynolds numbers.

1.1.3 Mixing Layer Instabilities

Flow instabilities can be found in mixing layers as well. The velocity profile of two parallel flows of different velocities (or densities) has an inflection point, which is a necessary condition for instability. The first to develop the equations for a mixing layer was done by Lessen (1950) who showed mathematically that for all flows, except very low Reynolds numbers, a mixing layer is unstable and he obtained the stability equation and reported the regions of stability and instability. Lock (1951) also conducted researching the area of instability of mixing layers but extended the stability equations to include fluids of different viscosities and densities. Betchov and Szewczyk (1963) examined the stability of a laminar shear layer of two parallel streams. They obtained, through numerical methods, neutral stability curves as well as curves of constant amplification for Reynolds numbers from 0 to 40 for viscous and inviscid cases. It was concluded that transition would occur at a Reynolds number of 150. Figure 1.4 shows the growth rate as a function of wavenumber for the laminar mixing profile.

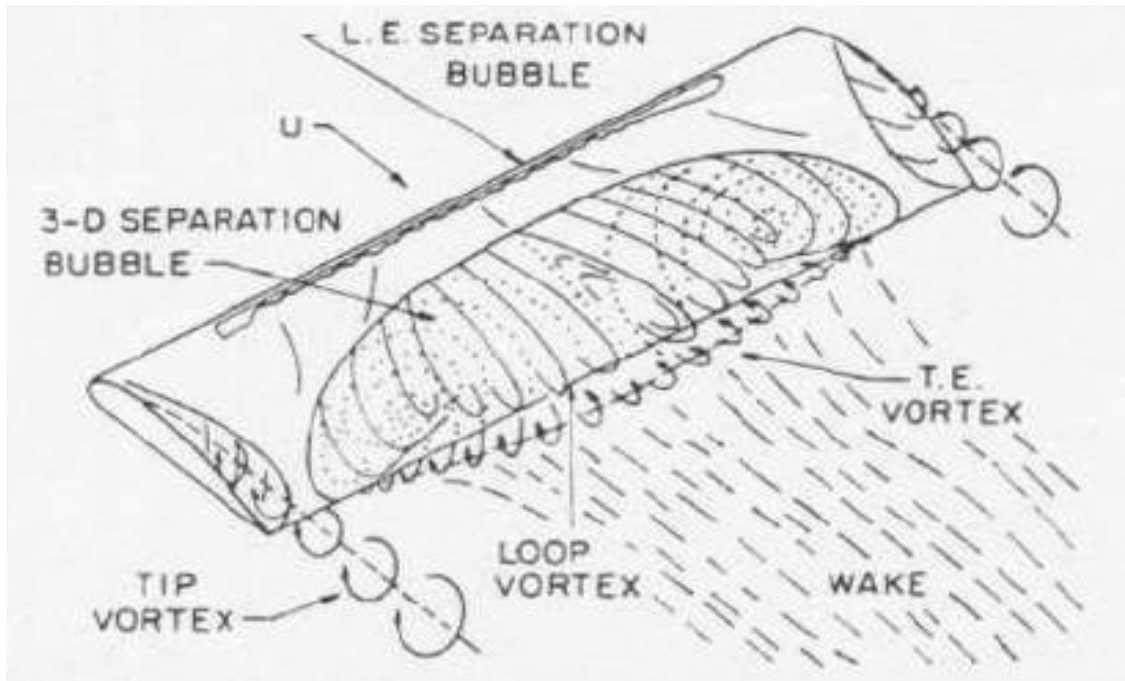


Figure 1.1 - Artistic representation of a low Reynolds number flow field over an airfoil (Bastedo and Mueller, 1986)

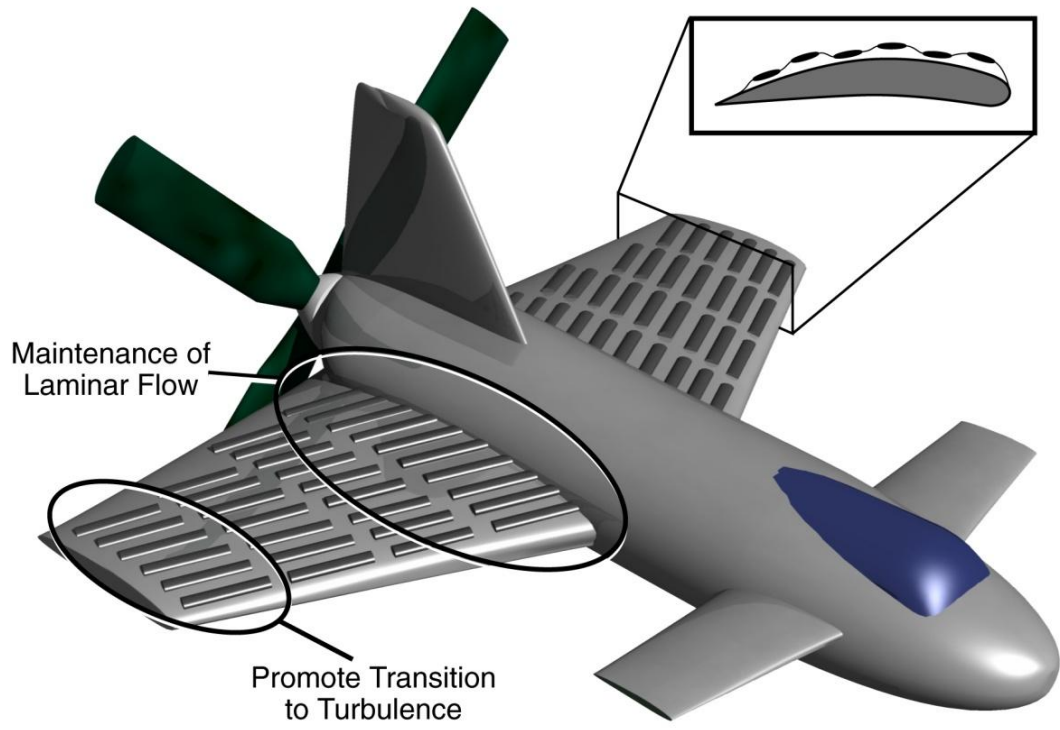


Figure 1.2 - Representation of an Electro-Active Polymer implementation on a MAV.

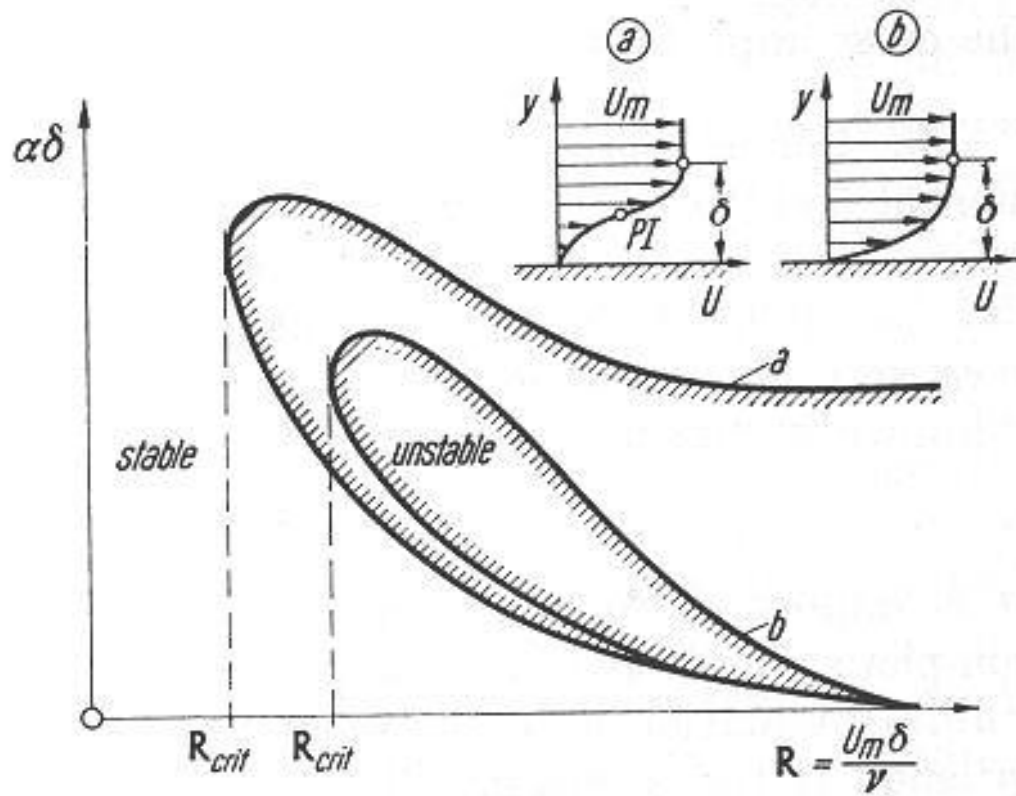


Figure 1.3 - Curves of neutral stability for 2D boundary layer for the (a) non-viscous instability and (b) for viscous instability (Schlichting, 1979, pp.461)

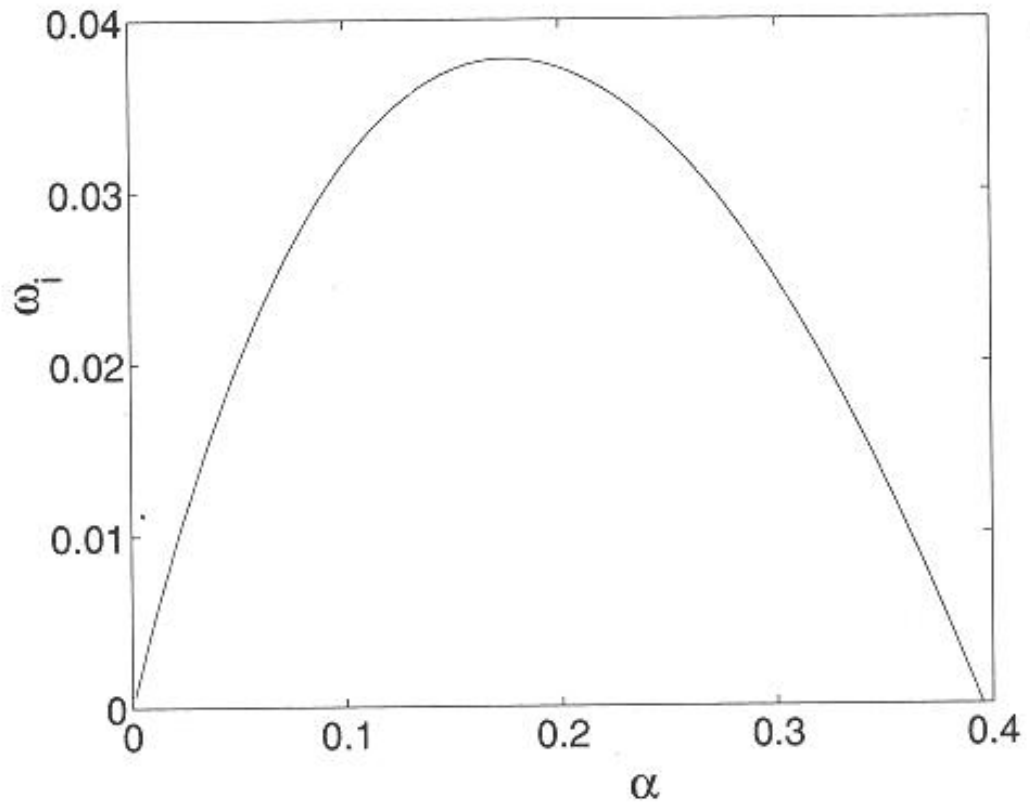


Figure 1.4 - Growth rate as a function of wavenumber for a laminar mixing layer profile(Criminalle et al., 2003, pp.67)

1.1.4 Laminar Separation Bubbles

The behavior of laminar separation bubbles has been a topic of research for decades and can provide insight into flow control within a mixing layer with or without flow separation. Gaster (1967) conducted an extensive study on the behavior of separation bubbles over a wide variety of Reynolds numbers and pressure gradients using hot-wire measurements. The goal of his experiments was to find criteria for predicting which form of separation bubble is most likely to appear in any given situation. He found that the bubble structure depended on both the Reynolds number as well as the pressure rise over the region of the bubble. He also found that a short laminar separation bubble can undergo a “bursting” which lead to either a long separation bubble or full separation, and the circumstances and behaviors of this bursting. Diwan and Ramesh (2007) discuss the size and shape changes in LSB on a flat plate as the free stream velocity changes. As the Reynolds number decreases it was shown that the height of the separation bubble increased at a greater rate than its length.

1.1.5 Flow Control of Laminar Boundary Layers

Understanding the physics of flow control in laminar boundary layers under an adverse pressure gradient is crucial in the choice and application of the flow control device. Marxen et al. (2006) took an in depth look into the control of a LSB based on linear stability theory. They found that there are frequencies that can be used to reduce the size of a LSB and discussed how the size of the bubble effects. The authors stated that for larger bubbles the region of instability is larger and the most amplified frequency becomes larger. They also report that the only time the triggered instability mode was the cause for transition and reattachment was when that was in the region of the most amplified frequency. Triggering outside this frequency region did not cause earlier transition. They also found that separation bubbles and wake dynamics could be decoupled and studied independently. Diwan and Ramesh (2007) discussed the effect that infinitesimal and finite disturbances, created by a loudspeaker, on the separation bubble. They showed that finite amplitude forcing caused the bubble to reduce in size, and even infinitesimally small disturbances could control the size of the bubble.

Marxen et al. (2003) looked at the transition to turbulence inside a LSB followed by reattachment using experimental and numerical techniques. The development of small disturbances, corresponding to Tollmien-Schlichting instabilities, was analyzed along with their role in the breakdown to turbulence. This study was extended by Lang et al. (2004) using stereoscopic Particle Image Velocimetry (PIV) and Laser Doppler Anemometry (LDA) to analyze the transition mechanisms in laminar boundary separations. They found that the 2D TS waves were the main factor in determining the size and position of the LSB, and the disturbances in the streamwise direction only played a minor role in the transition process.

Abdullah et al., (2009) discussed the possibility for shape memory alloys to be used as a flexible skin for variable camber airfoils. A shape shifting airfoil possesses many benefits in flight, allowing the optimization of lift-to-drag ratios for all flight conditions. Udovidchik and Morrison (2006) investigated the effects of dimple actuation on separating laminar and turbulent boundary layers. The dimples were oriented spanwise on a cylinder and the separation location for different frequencies was analyzed. They showed that in the region of the dimples, actuated at 10 Hz, the cylinder separation was delayed much dedicated to the production of streamwise vortex pairs, which has been seen to prevent separation in numerous works (e.g., Amitay et al., 2001).

Goksel (2007) conducted an in depth study of the effect of plasma flow control at lower Reynolds numbers ($20,000 < Re < 140,000$). They found that utilizing plasma-based flow control on an Eppler E338 airfoil significantly increased the lift characteristics of the airfoil. A study on the duty cycle of the control waveform found that an actuation duty cycles as low as 0.66% was still effective in separation control.

2. EXPERIMENTAL SETUP

2.1 Wind Tunnel Restoration

For the present project an old small-scale wind tunnel was available for the experiments. However, the facility was in a bad shape and had to be renovated. The tunnel was classified as a low Reynolds number suction system, where the turbine was located the downstream of the test section (Figure 2.1). Following the renovation the tunnel produced velocities between 0.5m/s to 30m/s with less than 0.5% free stream turbulence intensities over the velocity range. It is important to note that low frequencies (high-pass filter set to 5Hz) were filtered from all the data acquisition due to a structural vibration induced from the motor.

2.1.1 Inlet

The inlet of any wind tunnel is very important in keeping the turbulence intensity of the flow low enough to meet the standards of the experiment because all the disturbances induced by the inlet will propagate downstream into the test section. The converging section of this wind tunnel needed quite a bit of work before it was usable. Its dimensions consisted of a 20" x 20" inlet that converged to a 4" x 4" section. The convergence followed a 5th order polynomial over a length of 24", with the boundary conditions consisting of the first and second derivatives of the polynomial equal to zero at the ends.

At the time the tunnel was acquired the only flow straightening was done by hundreds of stacked plastic straws to mimic a honeycomb system, which can be quite effective and cheap if applied correctly. It was decided that this section should be replaced with an aluminum honeycomb and steel screen system. Two honeycombs were acquired for the inlet, one piece that has 0.125" diameter holes and 1" in thickness, and the other with holes of 0.25" diameter and 5" of thickness. Each honeycomb section also had a steel screen associated with it cut from a corrosion-resistant type 304 SS wire cloth, 70 x 70 mesh per 12" x 12" square sheet, with 0.0065" diameter wires. The screens were sown to the honeycomb using a needle and thread, which allowed the screen to be pulled tight before attaching to the honeycomb ensuring that the screen and honeycomb were stable in the tunnel.

The converging section was also fit with pressure rings at both ends. The rings consisted of static pressure ports flush with the surface of the tunnel on all four walls. The connection of the pressure ports to one pressure ring allowed an average pressure reading over all four walls. Each pressure ring was connected to a SETRA differential pressure transducer, ranging from $\pm 50''$ WC with an accuracy of $\pm 0.5\%$ full scale. With the two pressure readings the tunnel's velocity could then be derived using Bernoulli's equation along with conservation of mass flow rate (assuming density is constant). This provided an accurate velocity reading for the experiments as well as something to calibrate a hot-wire to inside the wind tunnel.

2.1.2 Test Section

The test section that came with the wind tunnel was absolutely in need of replacement for our project. An entire new test section was designed and machined from clear cast acrylic. The machining was completed by Tyler Van Buren, with the assistance of the licensed machinist David Digiulio when it was needed. The new test section has a square cross section of $4'' \times 4''$ and $20''$ long. The walls are $\frac{1}{2}''$ thick, with one wall designed to be removed easily. The side walls were designed to accommodate the experimental apparatus, and the suspended flat plate (described in detail later on). Two tops were designed and manufactured, one kept perfectly clear and uncut for PIV measurements, and one was designed with a small slit in the top with brushes to allow a hotwire to traverse streamwise as well as up and down. The test section attached to the exit of the converging section and the inlet of the diverging section through two endplates for mating. Refer to Figure 2.2 to view the completed test section with the experiment installed.

2.1.3 Outlet

Although not as important to the flow field quality, the outlet section (the portion downstream of the test section) has many necessary functions that made the tunnel at the proper quality. The outlet section provides the power source for pulling the air through the tunnel, diffuse the air, as well as other aspects. The outlet of the tunnel consists of the diverging section and the turbine housing.

The diverging section (diffuser) starts with the 4" x 4" square cross section that diverges to a 16" diameter exit over the length of 55", made out of wood. The shape transformation is done for the purpose of connecting the diffuser to the round turbine housing. Upon inspection of this section it was deemed fit for experimentation without any added parts, but some sanding and wood putty replacement was performed.

The turbine has two different subsections; following the diverging section there is a small straight section 16" in diameter and 18" in length, which consists of a plastic honeycomb as well as a divergence cone. The purpose of this section is to condition the air for the turbine itself, using the honeycomb to eliminate any large flow structures that could propagate upstream. The cones purpose is to diverge the air to the outside of the axis of rotation of the turbine, this ensures that all the air passes through the turbine section uniformly, with little disturbance due to the turbine axis. Although all of these components were satisfactory for experimentation, a rubber piece was added between this straight section and the turbine section to minimize structural vibrations that propagate from the turbine to the test section. This and sanding raised the section to the required experimental standards.

Following the straight section is the steel section that houses the turbine as well as the motor and its controller. Upon receiving the turbine housing the only working part was the turbine itself (after some greasing); no working motor or controller could be salvaged and thus had to be replaced. The controller is a Delta VFD-B model controller, which drives a 3 HP/60Hz electric 3-phase motor. The motor attaches to the turbine rotation axis from the outside through two drive belts. To make the electronic noise emitting from the motor acceptable the carrier frequency had to be maximized, which in turn resulted in a high pitched audible noise when the tunnel runs. At the end of this turbine housing is another diverging section, which goes from 16" to 20" in diameter over 36" of length. Another honeycomb with 0.25" diameter holes and 5" thick was added to the end of this diverging section purely to add a pressure drop to the system allowing for a much lower stable velocity limitation.

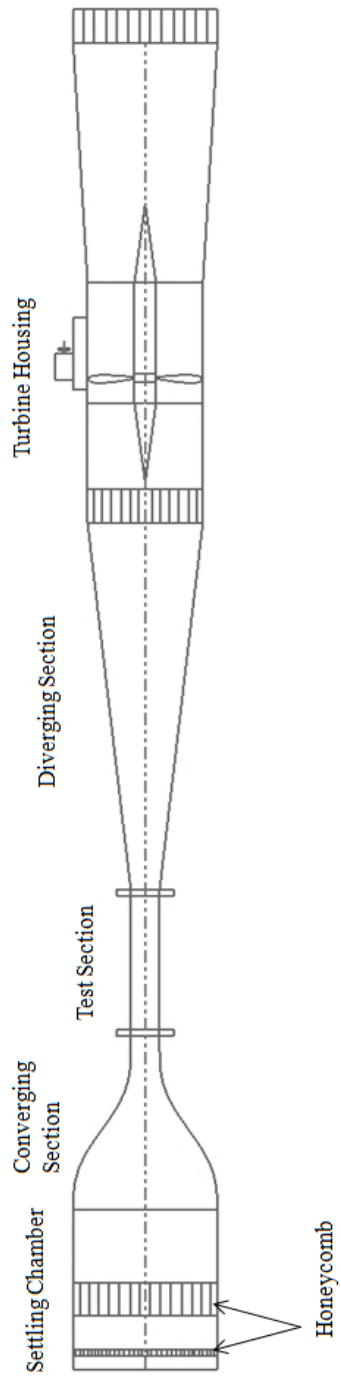


Figure2.1 - Wind tunnel schematic

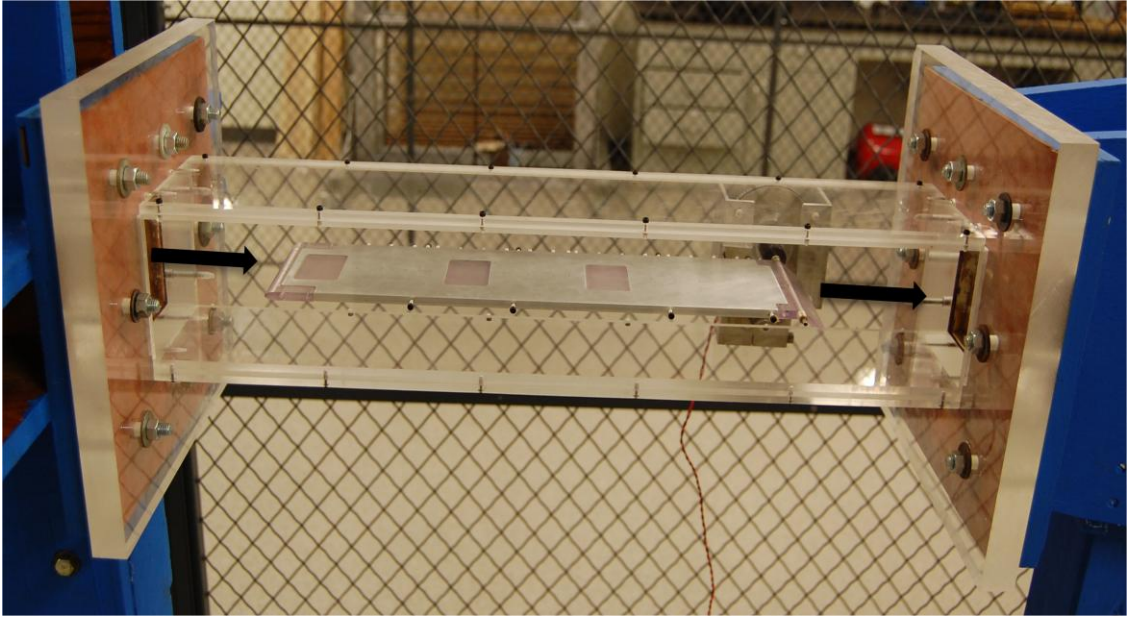


Figure 2.2 - Test section

2.2 FLAT PLATE DESIGN

With the main goal of determining whether the EAPs could successfully alter the boundary layer at lower Reynolds numbers it was clear that a special system needed to be designed for the tunnel's test section. This system needed a way to adjust the streamwise pressure gradient with the hopes of creating a controlled laminar separation bubble. Common techniques to achieve that are a variable walled test section (e.g., Diwan and Ramesh, 2007) and an adjustable flap on the back end of the plate. In the present work, the latter solution was used (Figure 2.3).

2.2.1 Flat Plate

The main portion of the flat plate is constructed from aluminum and machined in RPI's facilities. The plate was 15" in length (not including leading edge and flap), 4" wide, and 0.25" thick. The surface roughness of the plate is N8 grade. The plate incorporated holes along the centerline (pressure ports) for surface pressure readings as well as holes on the side for wind tunnel mounting. On the leading edge and trailing edge of the plate are cuts to house a leading edge and flap mating piece, as well as cutouts in the center to hold the EAP plug pieces.

2.2.2 Leading Edge

As was shown by multiple researchers (Narasimha and Prasad, 1994), the leading edge geometry proves to be quite important even when designing the most basic wind tunnel models like a flat plate. It was decided that an elliptical leading edge (3:1 axes ratio) would be best suited for the experiments due to its characteristics of minimizing local flow separation at the leading edge. The leading edge was fabricated from SLA (stereolithography 3D printing) and mated with the aluminum flat plate through countersunk bolts on the sides.

2.2.3 Flap

As mentioned above, the streamwise pressure gradient in the test section was obtained using a flap deflected on the back end of a flat plate. A PennEngineering stepper motor coupled with a US Digital encoder was chosen to enable the flap deflection (Figure 2.5).

This was run through a Matlab program designed to deflect the flap over a range of $\pm 45^\circ$ with an accuracy of 0.1° . The purpose of having this complicated system for static flap deflections is to enable future experiments with dynamic flap deflections.

Along with the angular adjustment capabilities of the flap it was decided that multiple flap sizes would be fabricated to allow for a large range of pressure gradients. Three flaps were constructed from SLA consisting of 1", 1.5", and 2" lengths. The flap cross sectional geometry consists of a 0.25" diameter semi circle mated with an isosceles triangle with an altitude defined by its length. The flap rotates about the center of the half circle. The versatility of the flap size as well as deflection angle allows for the ability to accurately create and control a laminar separation bubble on the flap plate.

2.2.4 EAP Plugs

In the present work the EAP was used as the flow control technique and its performance directly affects the success of the project making its application to the flap plate an important aspect of the design. Three locations were chosen for the ability to house one EAP in different locations or multiple EAPS at one time. The three locations are 1.25", 5.75", and 10.25" from the tip of the leading edge to the center of the EAP (see Figures 2.3 and 2.4).

For each location two plug pieces were designed and constructed. One piece was used as a dummy plug, which when fixed to the aluminum plate via the cutouts would act as a flat surface with minimum disturbance to the flow. The other piece was designed almost exactly as the dummy plug with the accommodation for an EAP by a recess cut into the surface. The thickness of these plugs varied based on EAP design, but the width and length remained constant at 1.32" and 2.05", respectively. The pieces were constructed from SLA mainly because of the high voltage and conductive properties of the EAP would not have paired well with conductive plug pieces.

2.2.5 EAP Devices

The EAPs themselves were fitted on the top of the plugs. In the present work, the EAP consisted of multiple layers, one being a polymer that reacts to an electric field by changing shape. Often times in the presence of an electric field the polymer will shrink,

and then will return to its original shape when the electric field is turned off. The other layers consist of insulators, a carbon sheet where the positive charge is applied, a plastic dimple sheet giving the deflection of the surface a decided shape, and an aluminum plate where the negative charge is applied (see Figure 2.6 for a schematic of the layer design method).

The hard plastic layer can be designed to meet the needs of any EAP application. The design is quite simple, any location where there is plastic the polymer won't be able to deflect in that area, and any area where there is no plastic the polymer will deflect. In the present work a specific dimple size and spacing was used, as shown in Figure 2.7.

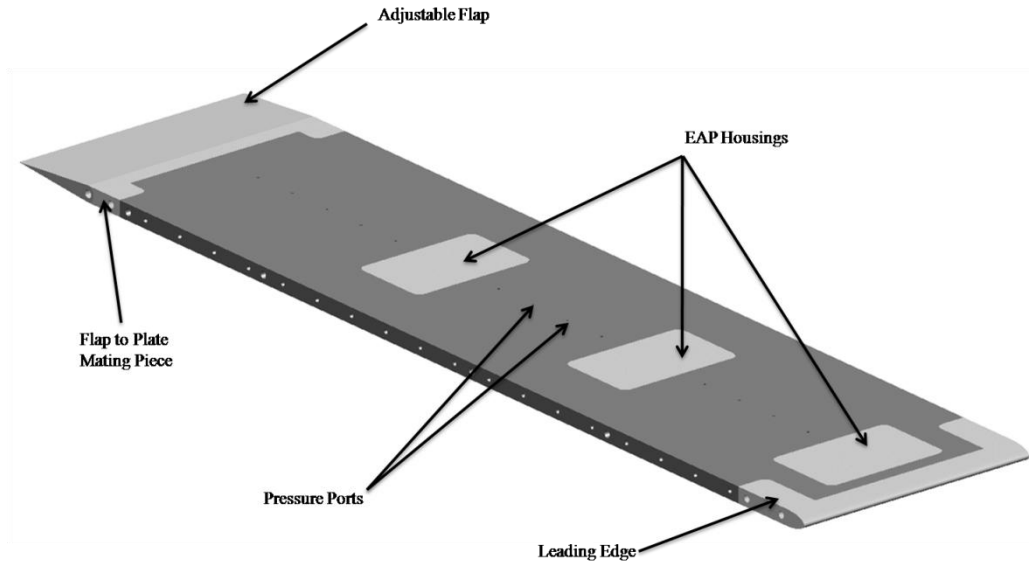


Figure 2.3 - CAD model of the flap plate design. Dark grey represents aluminum and light grey represents SLA

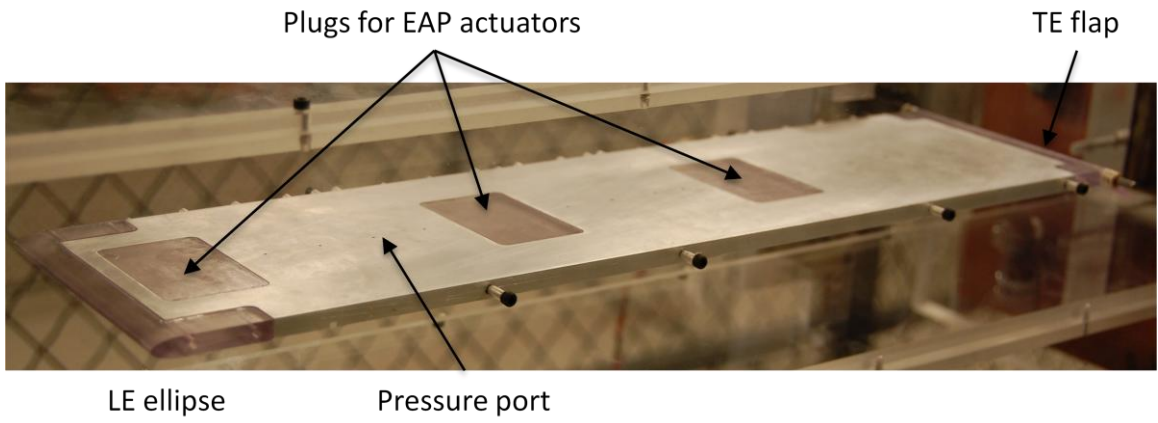


Figure 2.4 - Fabricated flat plate

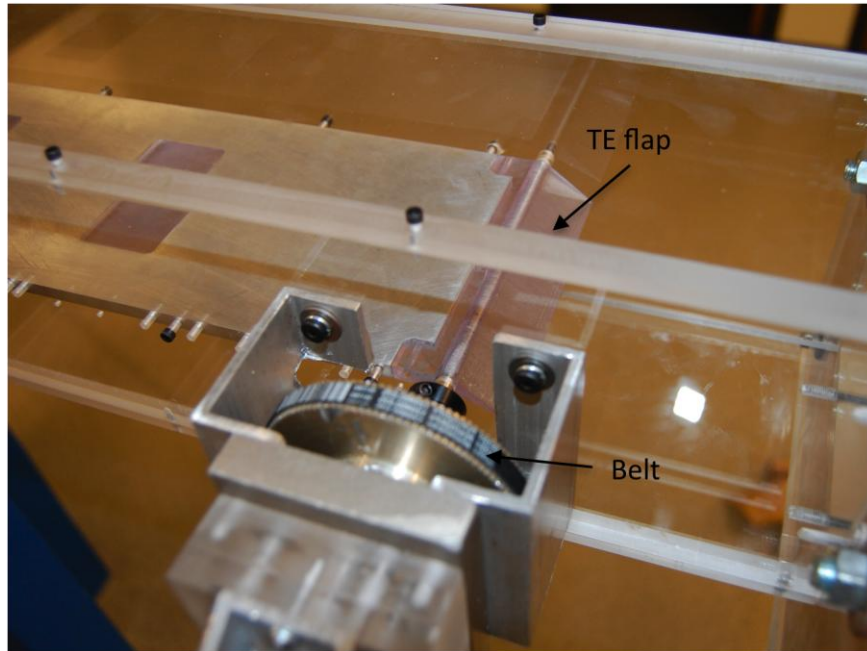


Figure 2.5 - Trailing edge flap and its mechanism

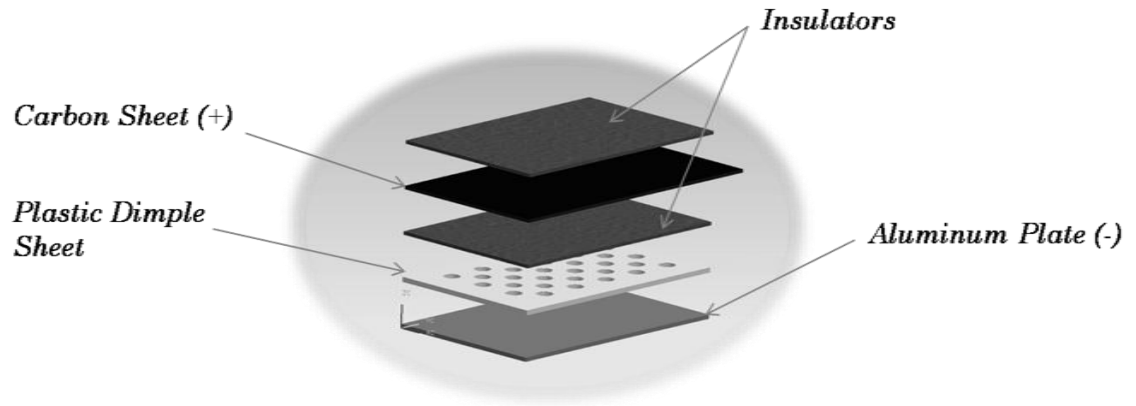


Figure 2.6 - EAP layer configuration, CAD representation

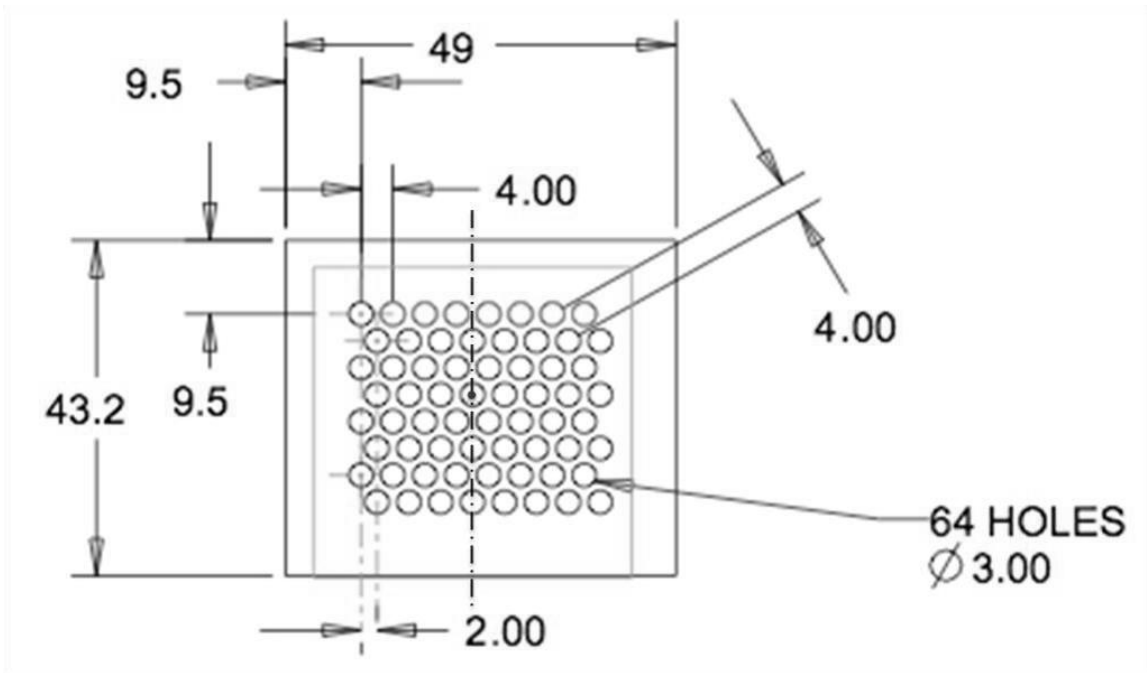


Figure 2.7 - EAP hole configuration

3. RESULTS

3.1 EAP CALIBRATION

Before utilizing the EAP actuators it was important to quantify their performance (e.g., driving frequency, input voltage, surface displacement, etc.). The EAPs are unique in a sense that the displacement frequency of the EAP is twice the driving frequency because the EAP deflects when either positive or negative input voltages are applied (the nature of the EAP is that a voltage difference causes the attraction).

In addition to measuring the EAPs frequency and displacement, their spatial displacement was measured and quantified. The EAPs were designed such that multiple dynamic dimples will be produced when a voltage was applied; however, due to a faulty glue application by the manufacturer the surface material of the EAP did not in fact deform solely at the dimple locations causing a parabolic surface deflection throughout the entire EAP surface. Figure 3.1 presents a surface deflection of the EAP (before the glue gave up); it clearly shows the formation of distributed surface deflection.

A Trek Model 609E-6 amplifier was used, coupled with an in-house LabView program (wave signal generator), to drive the EAPs at up to voltage amplitude of 2000V and driving frequencies up to 500Hz. A *Polytec: PDV 100* Laser Doppler Velocimetry (LDV) system was used to measure the velocity of the surface deflection. Using this velocity profile (Figure 3.2) and knowing the initial location of the EAP surface the displacement profile could then be integrated out and plotted as a function of time (done by an in-house LabView program). The dark surface of the EAP provided an ideal situation for the LDV minimizing reflection issues that are commonly seen with laser devices. The LDV was attached to a three-axis traverse system providing the ability to record the deflection of the EAP with a spatial resolution of 0.005". A picture of the experimental setup can be seen in Figure 3.3.

For the experiments an EAP with a substrate that incorporates 3mm diameter holes was chosen for calibration (see Figure 2.7 above). Both the 2D and 3D measurements were taken using the LDV on the traverse. Down the centerline points were taken every 0.1" (roughly 3mm) and the peaks were analyzed to give the maximum deflection. For the 3D measurements multiple planes were taken with the same spatial resolution.

The first experiment was a deflection profile averaged over three different EAP actuators to provide a correct average centerline deflection profile for the actuators used in the wind tunnel experiments. Two frequencies (50Hz and 150Hz) and two voltages (1000V and 2000V) were chosen to provide a good representation of the actuator behavior. Eight points were taken along the centerline, some over and some between the dimple areas. Figure 3.4 portrays the peak deflection profile, with deflections of up to 0.16mm. Clearly, the deflection is continuous throughout the EAP and does not depend on the holes on the substrate. This indicates that the designed dynamic roughness is not being added to the flow and that the actuator will need to be redesigned for further phases in the project. However, this EAP was still fine for the present work, as a pre-defined disturbance at different frequencies and amplitudes could be imposed on the flow. It can be seen that the driving frequency affects the deflection amplitudes; for a given input voltage, the higher frequency resulted in a higher peak deflection. It is possible to think of this oscillating device having a natural frequency that corresponds to the material properties and dimensions, so there would be a finite frequency that provides maximum amplitudes. Another observation is that the input voltage does not scale linearly with peak deflection. Double the input voltage yields nearly four times the peak deflection in both test cases.

In the present work, two sets of experiments at a voltage of 2000V were conducted, where the driving frequency was either 40Hz or 500Hz. These frequencies were chosen based on theoretical values of the flow instabilities as well as experimental values from the flow field. The 40Hz was chosen based upon the maximum amplified frequency over a flat plate for a given Reynolds number as derived from the Orr-Sommerfeld equation, or the TS waves. This theoretical value was supported when hotwire measurements yielded the same frequency in the flow above the flat plate. The 500Hz corresponded to the frequency that would be most amplified in the mixing layer calculated from the velocity profile at the point of inflection known as the Kelvin-Helmholtz waves. Figures 3.5 and 3.6 show 3 dimensional plots portraying the EAP deflection over the width and length of the actuator at for these two frequencies. These figures indicate that the EAP does not actuate in only the dimpled regions; rather, the entire EAP is deflected, as was discussed earlier. None the less the deflections of these

actuators are much higher than expected, providing up to 0.35mm peak displacement magnitude. With these displacements it was assumed (and proven, as will be shown later) that these EAPs would be affective in altering the boundary layer.

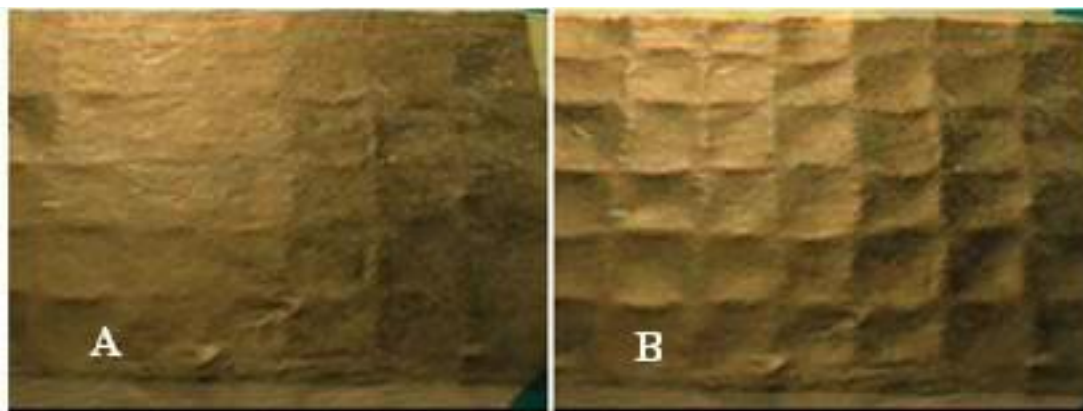


Figure 3.1 - EAPs surface: (A) unactuated, and (B) actuated

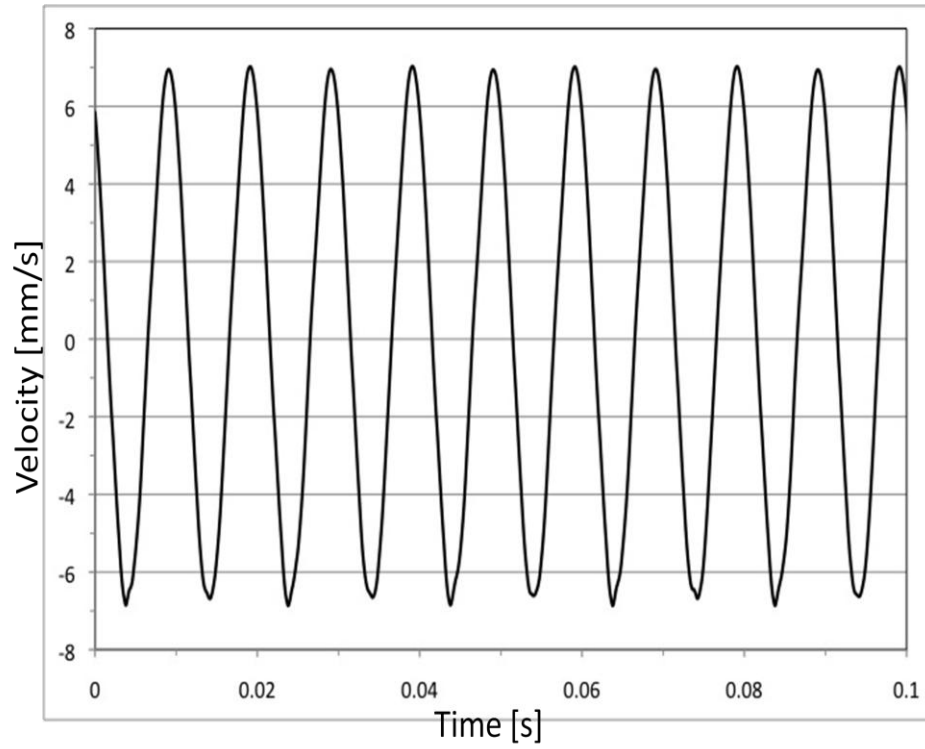


Figure 3.2 - Time varying of the EAP surface velocity; driving frequency is 50 Hz and input voltage of 2,000V

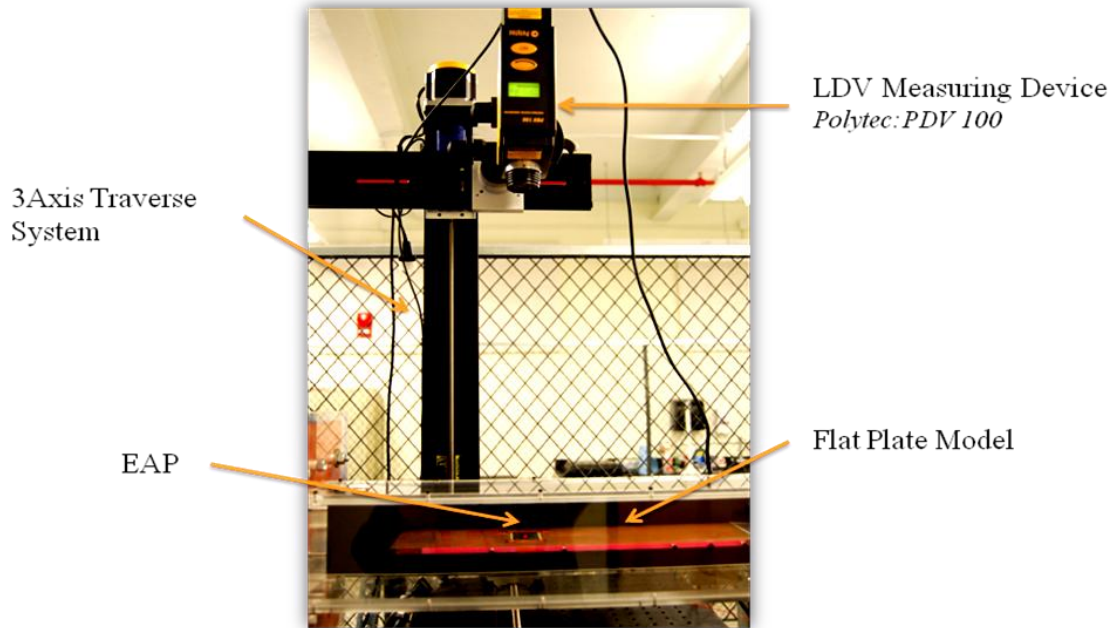


Figure 3.3 - LDV setup for the EAP calibration experiments

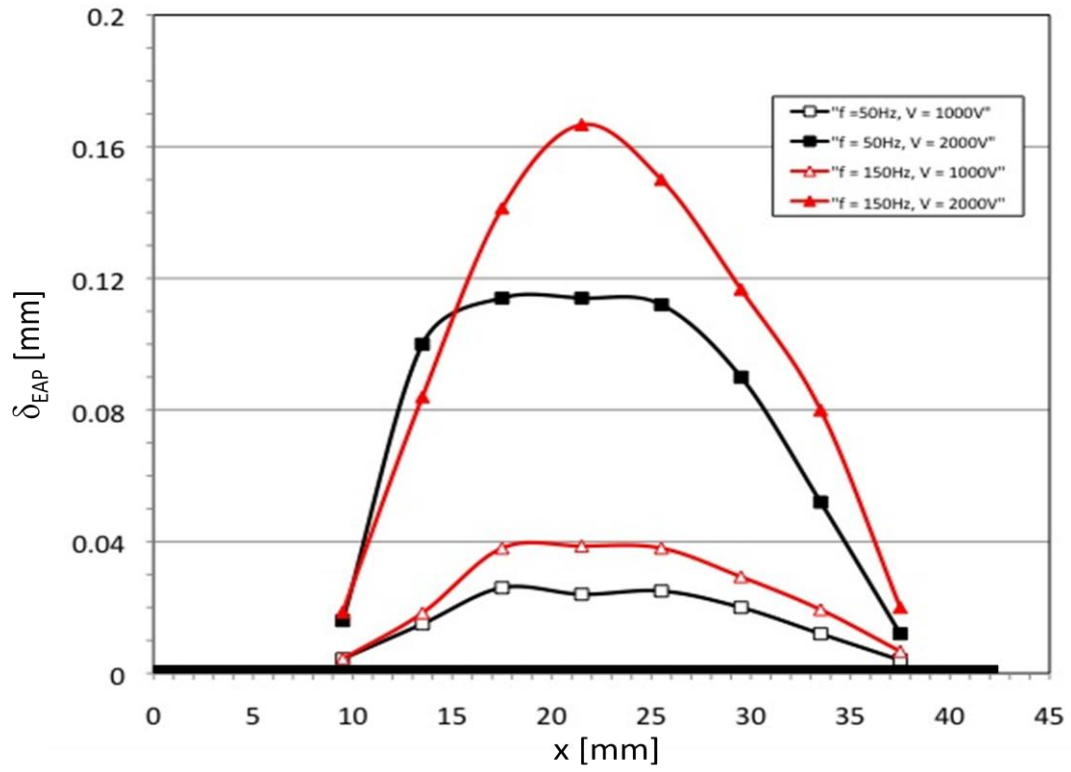


Figure 3.4 - Streamwise variation of the EAP displacement; driving frequency 50Hz and 150Hz, input voltage 1000V and 2,000V

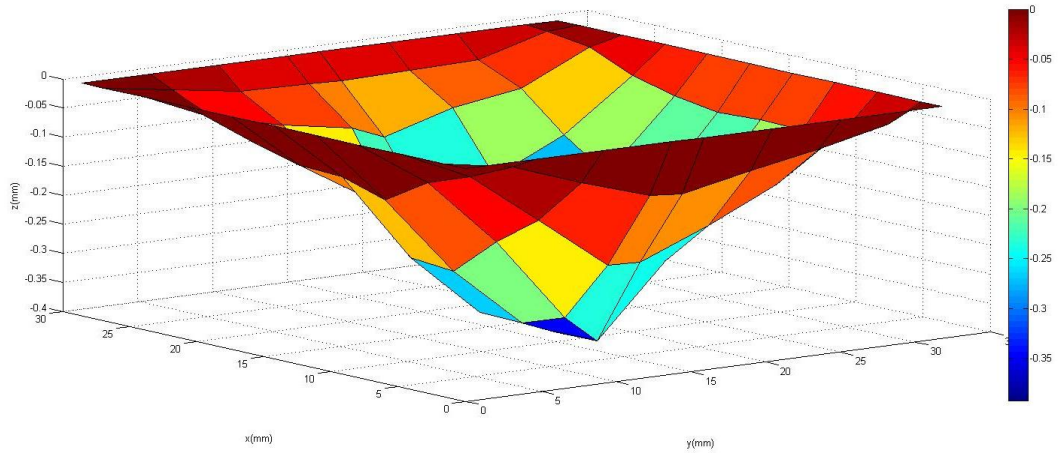


Figure 3.5 - 3D surface deflection at 40Hz and 2000V (the colors represent a different view of the vertical axis)

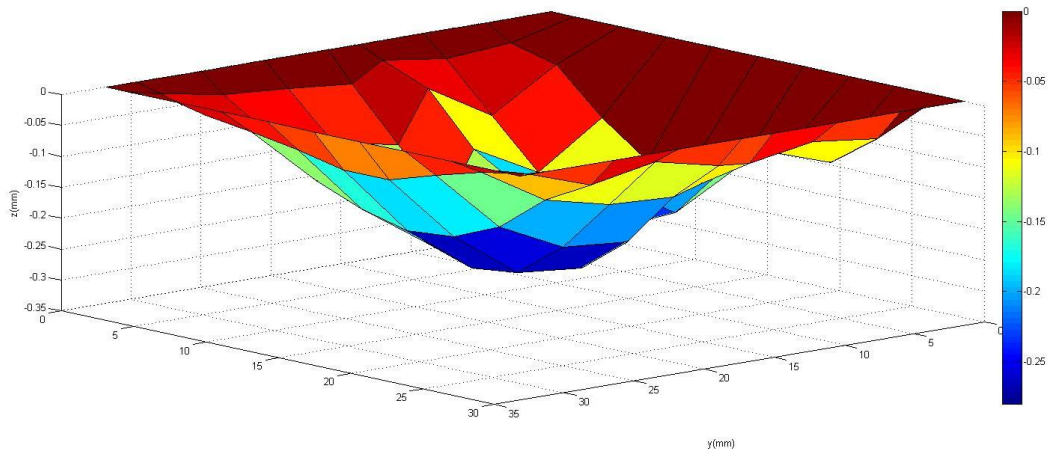


Figure 3.6 - 3D surface deflection at 500Hz and 2000V (the colors represent a different view of the vertical axis).

3.2 BOUNDARY LAYER MEASUREMENTS

Following the quantification of the EAPs boundary layer measurements, using a single hot-wire, were conducted to explore the feasibility of the EAP to alter the boundary layer. The theory and practice behind a hot-wire sensor is well known and documented (Bruun, 1995) and thus will not be described here in details.

A constant temperature hot-wire anemometry (CTA) utilizes a Wheatstone bridge circuit that is designed to keep a very thin tungsten wire (typically $5\mu\text{m}$ in diameter and $\sim 1\text{mm}$ in length) at a constant temperature by adjusting the bridge voltage. As air passes over the wire its resistance changes, and therefore the voltage required to keep the wire a constant temperature also changes. This voltage is correlated to the flow velocity accurately (up to 1% of the calibrated maximum) using a calibration procedure (the hot-wire calibration is discussed in the following section). This makes hotwire an ideal system for boundary layer measurements.

3.2.1 Experimental Procedure

The hot-wire anemometry system used in the present experiments was an A.A. Lab Systems LTD (model AN-1005) Anemometry System. A single hot-wire probe was installed in a test section with specially designed brushes to allow the hot-wire probe to move streamwise down the centerline, as well as being able to traverse normal to the plate. The motion was provided by two traverses similar to the ones used to hold the LDV. This setup allowed for precise boundary layer measurements to be made close to the wall, see Figure 3.7. The probe was angled in a way so that it was roughly 30 degrees from the plate jutting into the flow direction to reduce the intrusiveness of the probe with the flow measurements (see Figure 3.8 for a close look at the hot-wire probe on the flap plate).

For this experiment it was decided that the location of the EAP was to be placed in the middle housing the housing $5.125''$ from the leading edge. Two flap angles were chosen, corresponding to zero degrees and twelve degrees. The zero degree flap angle was chosen to show that the flat plate boundary layer followed the Blasius boundary layer solution (Schlichting, 1979) until transitioning to turbulence. The twelve degree

flap angle was chosen because it provided a downstream extent in the center of the plate where the boundary layer developed an inflection point, indicative of transition to a turbulent flow.

To quantify the incoming boundary layer at both angles it was helpful to compare them to the corresponding theoretical solutions for each circumstance. Figure 3.9 presents a comparison between the Blasius solution and the measured boundary layer at a streamwise location of 6.5" with a flap angle of 0°. Clearly, the incoming boundary layer compares quite well to the solution suggesting that boundary is laminar. Figure 3.10 presents the measured boundary layer profile at the same streamwise location but for the flap angle of 12° and is compared to the Falkner-Skan solution for a β of -0.05 corresponding to the measured pressure gradient across the plate. As can be seen, the comparison between the measured profile and the theoretical solution is poor, suggesting that the flow field is most likely transitional at that streamwise location. Furthermore, the presence of the inflection point yield flow instabilities similar to the one developed in a mixing layer (Criminale et al., 2003).

3.2.1.1 Hot-wire Calibration

The hot-wire calibration and the boundary layer experiments were conducted using LabView programs made in house. A free jet apparatus was used as the calibrator, where the hot-wire was calibrated against a velocity calculated from two SETRA +/- 50" WC pressure transducers, one at the inlet of the contraction and one at the jet exit plane. Using Bernoulli's equation one can calculate the velocity at the exit of the contraction with an accuracy of ~1% (White, 2006).

The calibration program was designed so that a minimum and maximum flow velocity were chosen, and seven calibration points in between this velocity range were measured so that a voltage vs. velocity curve could be constructed using a 4th order polynomial fit that would be accurate between the min and max velocities. The calibration coefficients of this polynomial were then stored in the computer and loaded for the various LabView programs that were used to determine the velocity at different locations in the test section.

3.2.1.1 Boundary Layer Experimental Procedure

The boundary layer measurement program was designed so that the hot-wire would be placed at a known location, at the leading edge 1" above the surface (in the free stream) and could be moved by computer driven traverse system down to any streamwise location. Then, the program would acquire the velocity using the hotwire (while also monitoring and recording the tunnel velocity) and then could be traversed down to predefined vertical locations above the surface to measure the boundary layer profile. The hot-wire output voltage was sampled at 5kHz for 30 seconds at each location, yielding roughly 150 thousand samples averaged to obtain one time-averaged velocity. The program also kept track of the probe location, free stream velocity, EAP frequency and voltage, and the ambient temperature at all times and recorded the information with the velocity data. These data were then stored and processed through a custom-made Matlab code for post-processing and final presentation. It is important to note that for every boundary layer profile the location of flat plate was obtained by extrapolating linearly from the last two data points in the boundary layer to zero velocity. This was done due to the inability for the hot-wire to get very close to the surface leaving out 10-20% of the boundary layer. This allowed for the alignment of all the boundary layers for comparison purposes.

3.2.2 Results and Discussion

3.2.2.1 Flap Angle Effect

Before testing the effect of the EAP on the boundary layer it was imperative to quantify the effect of the flap deflection on the boundary layer itself. This motivated an experiment to compare the baseline boundary layer (with the EAP installed but not deflected) to explore how the boundary layer develops with a flap angle of 0° as well as 12° . Data were taken at several locations: 6.5", 8.0", 9.5", and 12" from the plate's leading edge. This provided a good indication of the boundary layer development for both cases as well as targeted the area of the boundary layer along the plate that exhibited inflection points.

As shown in Figure 3.11, it can be seen that deflecting the flap downwards significantly changes the boundary layer profile. At the first downstream location it can

be seen that when the flap is deflected to 12° the boundary layer is pulled down as well as the presence of an inflection point near the top of the boundary layer. This indicates that the flow has started to transition to a turbulent boundary layer farther upstream on the flap plate (compared to the 0° case) due to the induced adverse pressure gradient. As the flow develops downstream the 0° flap angle case appears to grow in laminar fashion, whereas for the 12° flap angle the inflection point travels along the boundary layer and eventually at the 12.0" downstream from the leading edge the boundary layer resembles a turbulent boundary layer while the 0° case is still transitional. It is important to note that these boundary layers are in a transitional region and thus comparing them to theoretical solutions becomes irrelevant.

To describe the behavior of the baseline (no actuation) boundary layer (at 12° flap deflection) over the flap plate it is useful to look at the entire flat plate length with a few boundary layer profiles measured at different streamwise locations. Figure 3.12 presents the development of this boundary layer as along the plate through the adverse pressure gradient. Boundary layer measurements were taken at 0.75", 2.5", 4.5", 6.5", 7.5", 8.0", 8.5", 9.0", 9.5", and 12.0" providing a velocity profiles at multiple stages in the boundary layer development across the plate with higher spatial resolution at the points in the boundary layer with a strong inflection point. The line representing 95% of the free stream is also shown to depict the boundary layer thickness. It is clear that near the leading edge (at $x = 0.75"$, just downstream of the elliptical leading edge) the boundary layer has not quite developed fully because remnants of the accelerated flow over the curved surface can be seen, with velocities in the boundary layer being faster than the local free stream. By 2.5" downstream it is seen that a boundary layer that resembles a laminar boundary layer is formed and developed through 6.5".

As the flow transitions to a turbulent boundary layer it is seen that the boundary layer thickness increases drastically with plate downstream distance. Also the boundary layer profiles exhibit an inflection point for all of the boundary layers between $x = 7.5"$ to 9.5". These inflection points move upward as the downstream distance increases. At the last measured downstream location ($x = 12"$) the boundary layer appears to be turbulent without an inflection point in the velocity profile. These results indicate that if the EAP was to have a pronounce effect it would be when the boundary layer is most

unstable, which is the downstream extent where inflection points in the velocity profile are present.

3.2.2.2 Effect of the presence of the EAP

When installing devices for flow control into a flow field it is often overlooked the effects of the flow control device on the flow field without even being activated. The EAP, although designed to be flat and integrated into the plate surface had some flaws. The surface of the EAP was rubbery and inconsistent causing somewhat an induced roughness to the flow. Also, the material was somewhat loose on the surface so it was thought that a flow over it may cause some unintended vibrations of the surface inducing disturbances to the flow. From observation of these imperfections it was clear that an experiment needed to be conducted that quantified the effect the EAP had on the flow while unactuated. This unactuated case was used throughout the rest of the project as the “baseline” case.

Figure 3.13 shows the effects of the presence of EAP on the boundary layer development (compared to the “clean” case where a special SLA plugs were installed flush with the surface) over the plate at a 12° flap deflection. Boundary layer profiles were acquired at 6.5”, 7.5”, 8.0”, 8.5”, 9.0”, 9.5”, and 10” downstream of the leading edge. It is clear that the boundary layer development is affected by the presence of the EAP for the majority of the plate. At $x = 6.5$ ” downstream from the leading edge the EAP causes a thicker boundary layer, indicating that the transition process started closer to the leading edge (compared to the “clean” case). Farther downstream ($x = 7.5$ ” to 8.5”) the boundary layer is approximately the same, where both cases contain inflection points at about the same cross-stream location. At $x = 9.0$ ” and 9.5” the boundary layer seems to be more affected by the EAP presence; however, it might be within error of the linear extrapolation process used for aligning the boundary layers. Farther downstream, the boundary layers are almost identical, both turbulent as expected. This result indicates that although the presence of the (unactuated) EAP has some unintended effects, it can be assumed that the region of interest over the plate remains the same as the “clean” case, where the transition occurs between $x = 7$ ” to 10”.

3.2.2.3 Actuation Effects

Next, the effect of the actuated EAP on the evolution of the boundary layer was examined. The boundary layer at several streamwise locations was measured, including $x = 7.5''$ (A), $8.0''$ (B), $8.5''$ (C), $9.0''$ (D), $9.5''$ (E), $10.0''$ (F), and $12.0''$ (G). Note that these location labels are used for the rest of the figures in section 3.2.2.3. For each location both the normalized velocity profile as well as the turbulence intensity profile are presented. Figure 3.14 shows the unactuated boundary layer profile at different streamwise locations. It clearly shows that the vertical location of the inflection point varies as the location changes, with the last streamwise location being the turbulent boundary layer.

Figure 3.15 presents the turbulence intensity profile at the same streamwise locations as the velocity profiles for the unactuated case. As the streamwise distance from the leading edge increases the turbulence intensity increases, but it is also interesting to note that the turbulence profile becomes thicker from location (B) to (F), with the latter being the thickest. Even more interesting is that in the turbulent boundary layer, although the turbulence peak is higher, the cross-stream extent of the turbulence is smaller (it is a thinner boundary layer compared to the upstream locations).

Figure 3.16 shows of boundary layer profiles for the actuated case at a frequency of 40 Hz and input voltage of 2000V. Note that this frequency was selected to correspond to the TS waves. The boundary layer is slightly fuller (less velocity deficit) as the streamwise distance increases. When the actuation is applied the inflection point on the boundary layers profile are smoother than the unactuated case.

Figure 3.17 shows the turbulent intensity profiles of the 40Hz actuated case. From these plots it is hard to notice the effect of the EAP on the turbulence intensity; however, the effect of the EAP is much more pronounce when a driving frequency of 500Hz is used, as is shown in Figures 3.16 and 3.17. Figure 3.18 represents the velocity profiles at various streamwise locations. Note that the actuation frequency of 500Hz was selected to excite the inflection point-based instability. It is clear that this frequency has a pronounced and clear effect on the boundary layer profiles, as well as on the turbulent intensity (Figure 3.19).

To better appreciate the effect of the EAP on the flow field over the flat plate, the velocity and turbulent intensity profiles at $x = 8.0''$, $9.5''$, and $12.0''$ are presented in Figures 3.20, 3.21, and 3.22, respectively, where the baseline case is compared to the actuated cases (with 40Hz and 500Hz). At $x = 8''$, it is clear that the 500 Hz actuation case has the greatest effect on the boundary layer, successfully pulling the boundary layer closer to the surface, whereas the 40Hz actuation seems to have little to no effect at this streamwise location. Furthermore, 500Hz actuation has a significant effect on the turbulence intensity profile with almost double the “width” of region with high turbulence. It seems that although the 500Hz actuation lowered the peak turbulence intensity as it broadened it and pulled it closer to the surface. The peak turbulence for the 0 and 40 Hz case were roughly 10%, and 8.6% for the 500 Hz case. Farther downstream (at $x = 9.5$, Figure 3.21) the 500Hz actuation again has the most effect on the velocity profile, where the inflection point is mitigated. This suggests that the transition to a turbulent boundary layer is promoted. On the other hand, the 40 Hz actuation again having little to no effect indicating that the TS waves are being dominated by the already transitioning flow. This could mean that in order for the TS waves to be more effectively amplified the EAP needs to be actuated farther upstream from the region of interest. Moreover, the turbulence intensity profile is affected mainly by the 500Hz actuation, where the peak is closer to the surface. At this location the peak turbulence seems to be close to equal for each case at roughly 12%. The last location is presented in figure 3.22 representing the $12.0''$ location.

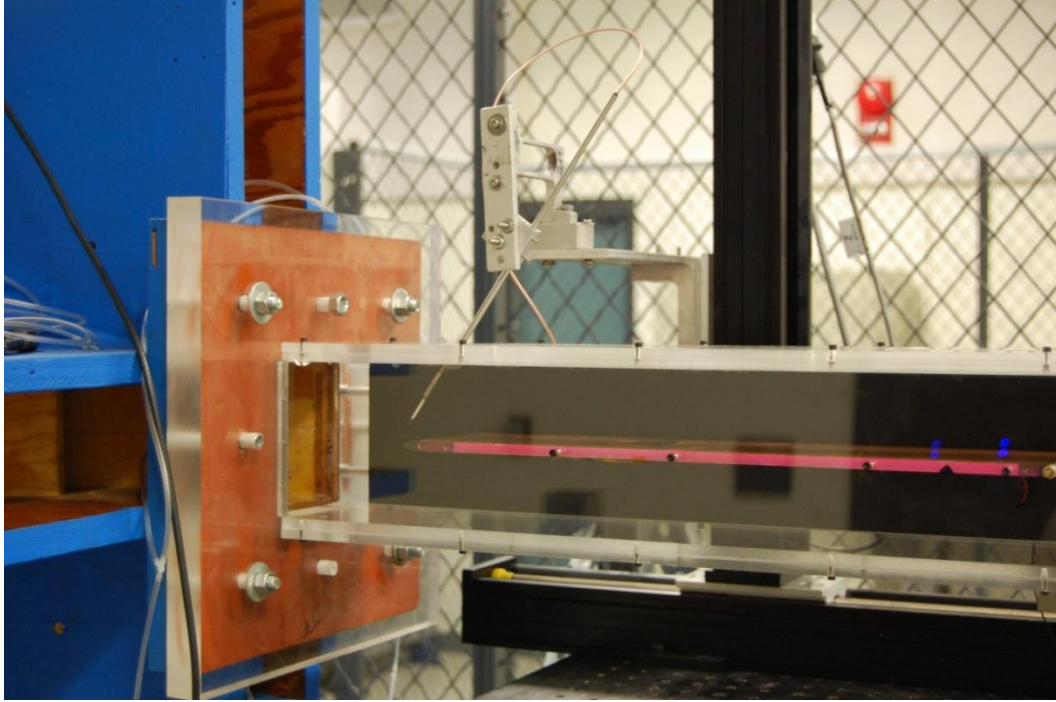


Figure 3.7 – View of the hotwire probe in the test section equipped with the flat plate

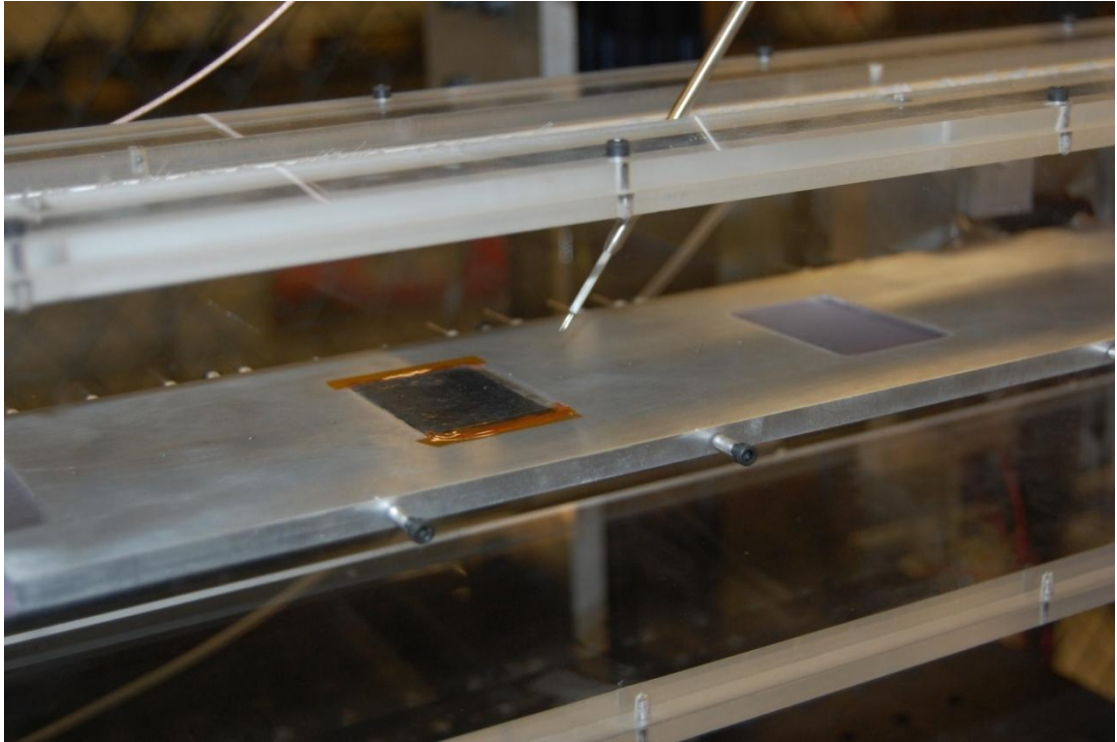


Figure 3.8 - Close up view of the hot-wire in the wind tunnel, EAP installed

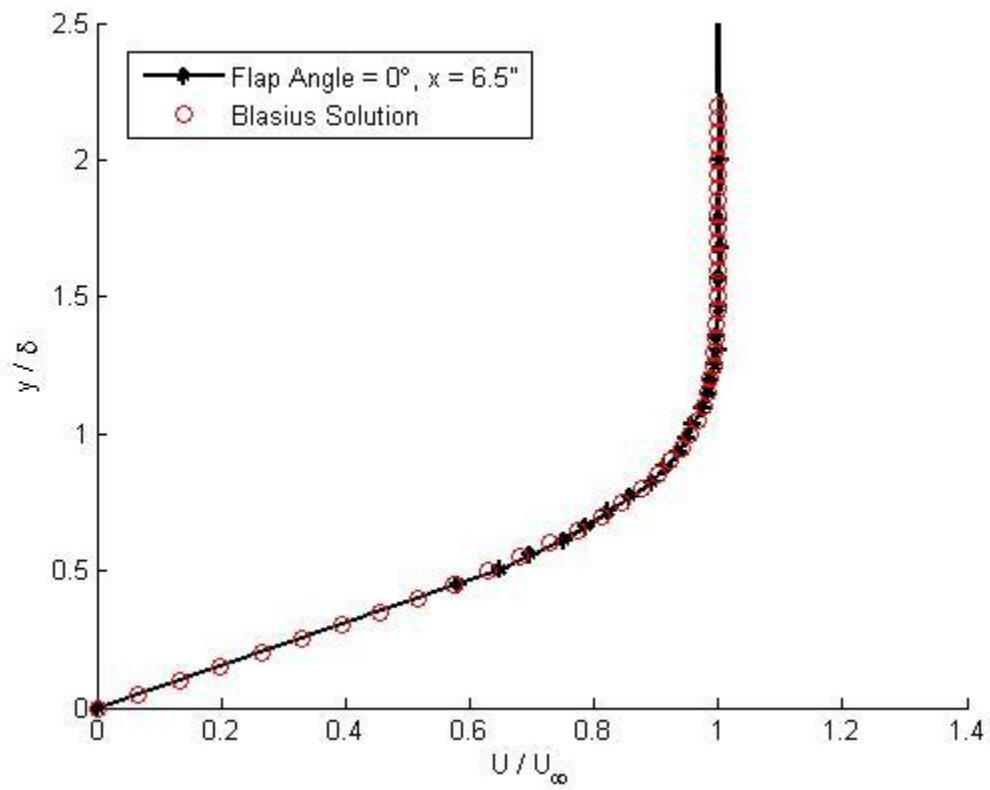


Figure 3.9 - Boundary layer comparison to the Blasius solution, streamwise location 6.5", flap angle 0°

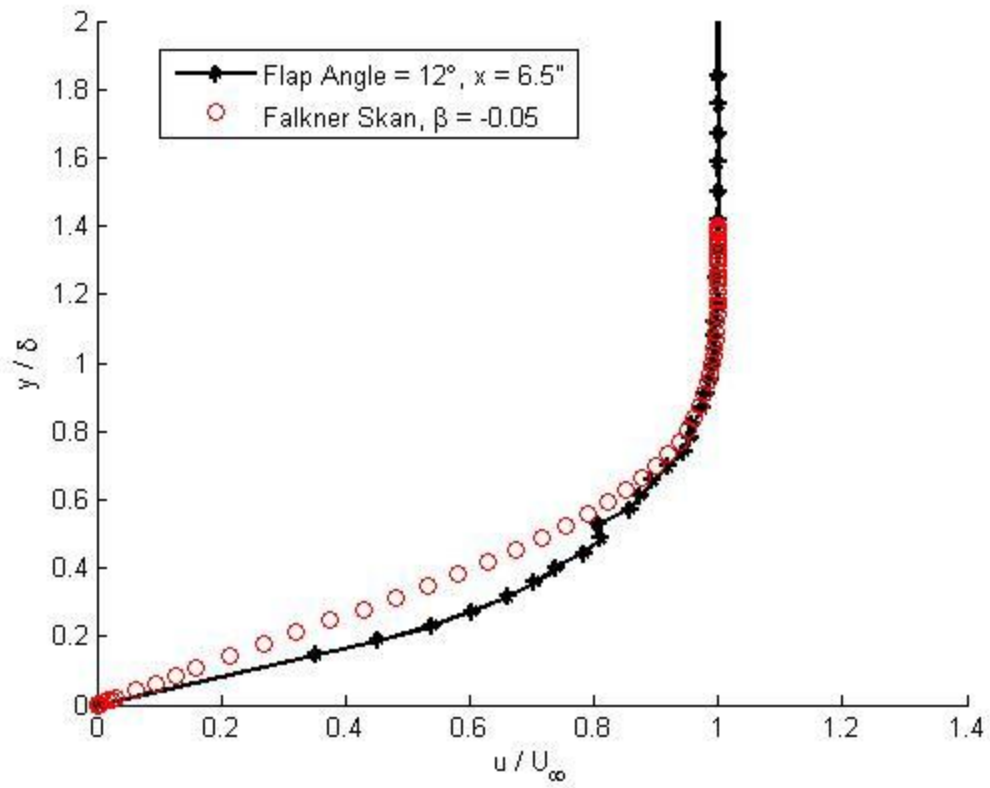


Figure 3.10 - Boundary layer comparison to the Falkner-Skan solution for $\beta = -0.05$, streamwise location 6.5", flap angle 12°

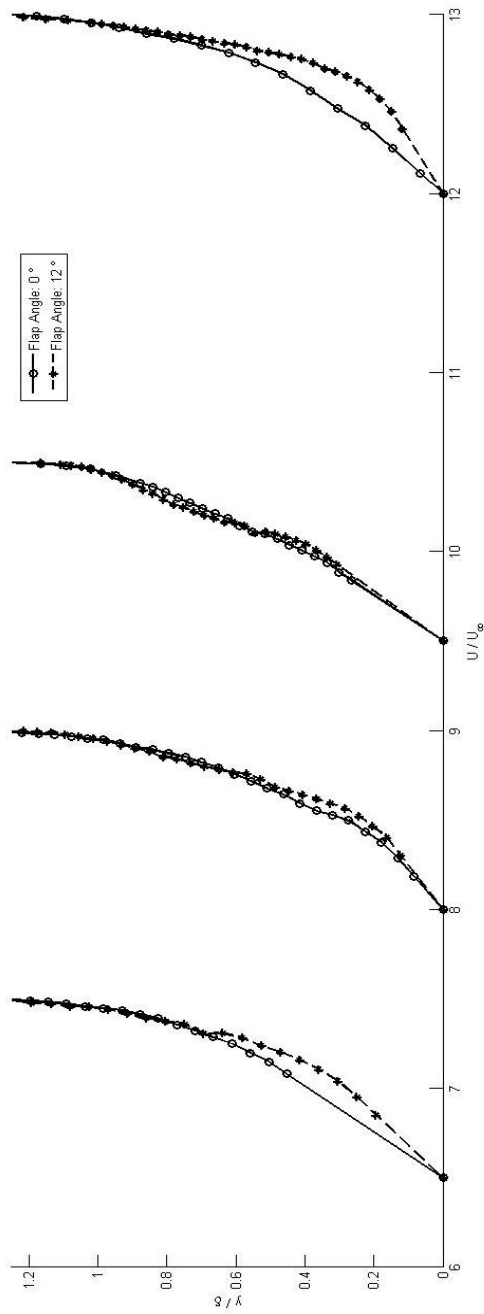


Figure 3.11 - Normalized boundary layer profiles offset by their streamwise location from the plate leading edge for two flap deflections: 0° and 12°

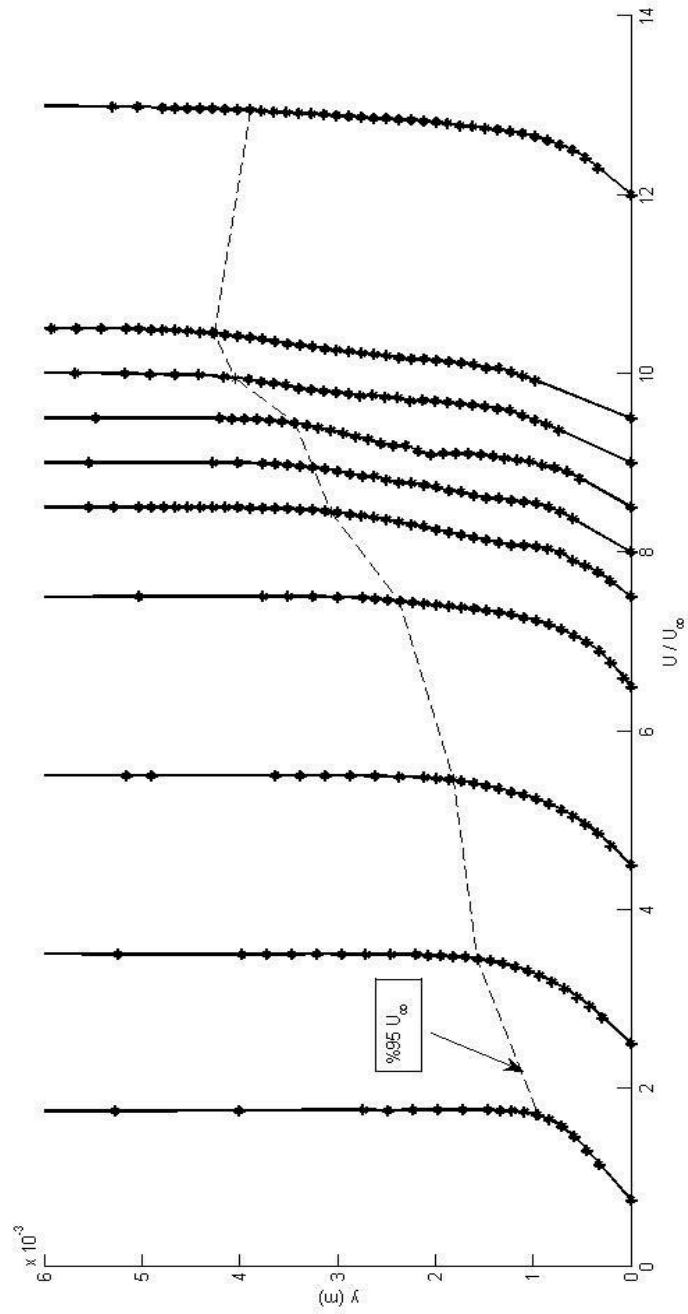


Figure 3.12 - Boundary layer evolution, flap angle 12°, normalized velocity offset by streamwise location from the leading edge, 95% U_∞ line included

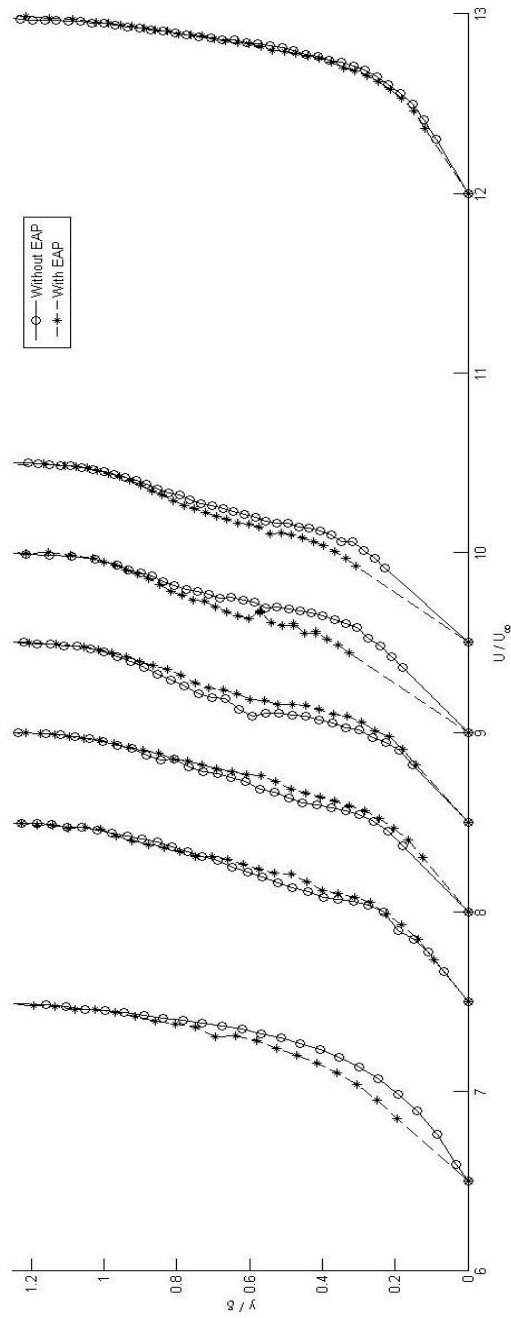


Figure 3.13 - Normalized boundary layer profiles offset by different plate locations, with and without EAP installed and un-actuated

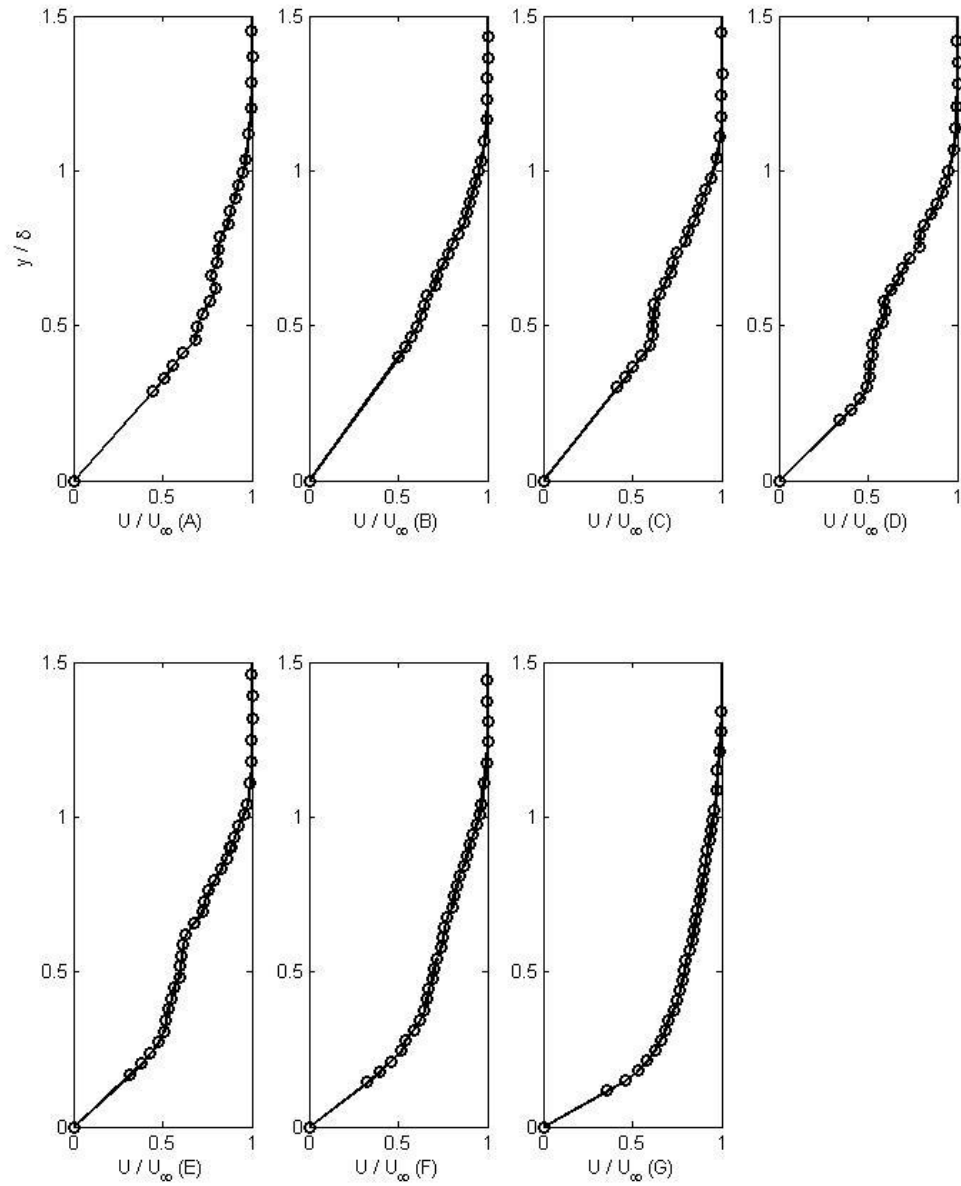


Figure 3.14 - Normalized boundary layer profiles, baseline (unactuated), different streamwise locations (A) 7.5", (B) 8.0", (C) 8.5", (D) 9.0", (E) 9.5", (F) 10.0", and (G) 12.0"

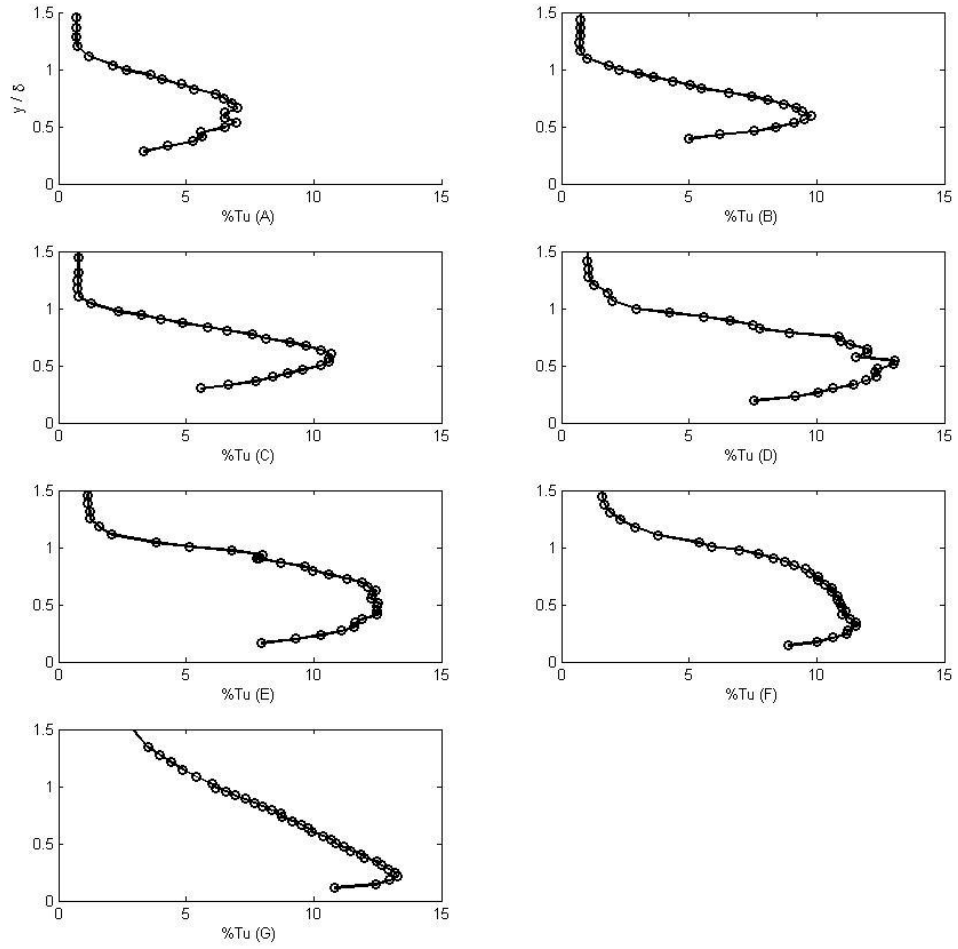


Figure 3.15 - Turbulence intensity profiles, baseline (unactuated), different streamwise locations (A) 7.5", (B) 8.0", (C) 8.5", (D) 9.0", (E) 9.5", (F) 10.0", and (G) 12.0"

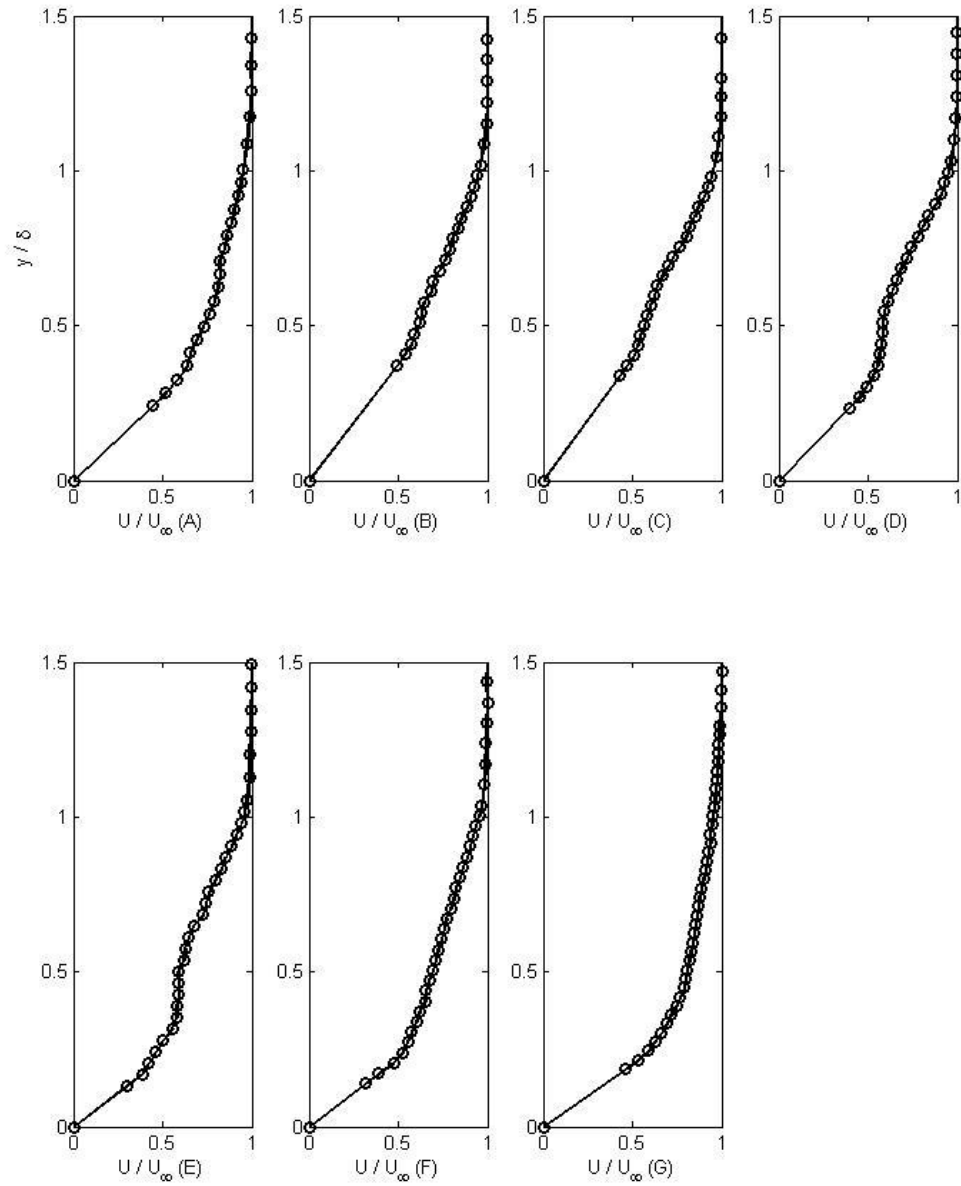


Figure 3.16 - Normalized boundary layer profiles, actuation frequency = 40 Hz, different streamwise locations (A) 7.5", (B) 8.0", (C) 8.5", (D) 9.0", (E) 9.5", (F) 10.0", and (G) 12.0"

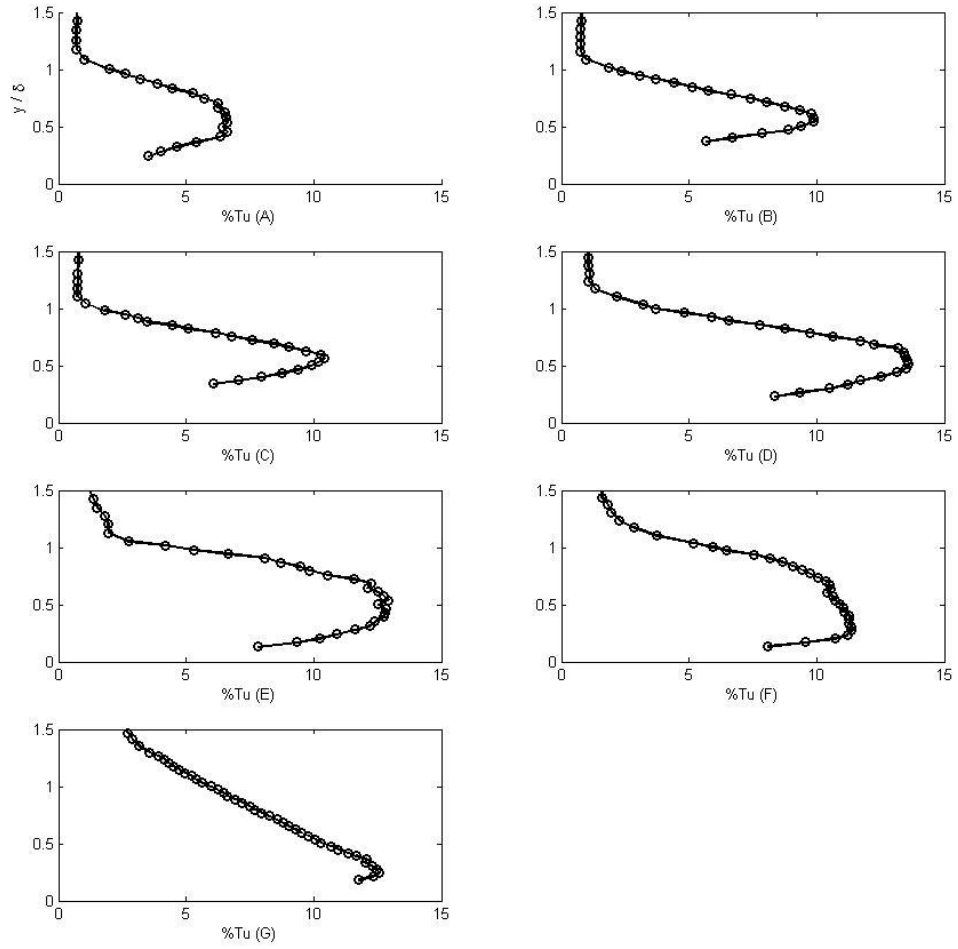


Figure 3.17 - Turbulence intensity profiles, actuation frequency = 40 Hz, different streamwise locations (A) 7.5", (B) 8.0", (C) 8.5", (D) 9.0", (E) 9.5", (F) 10.0", and (G) 12.0"

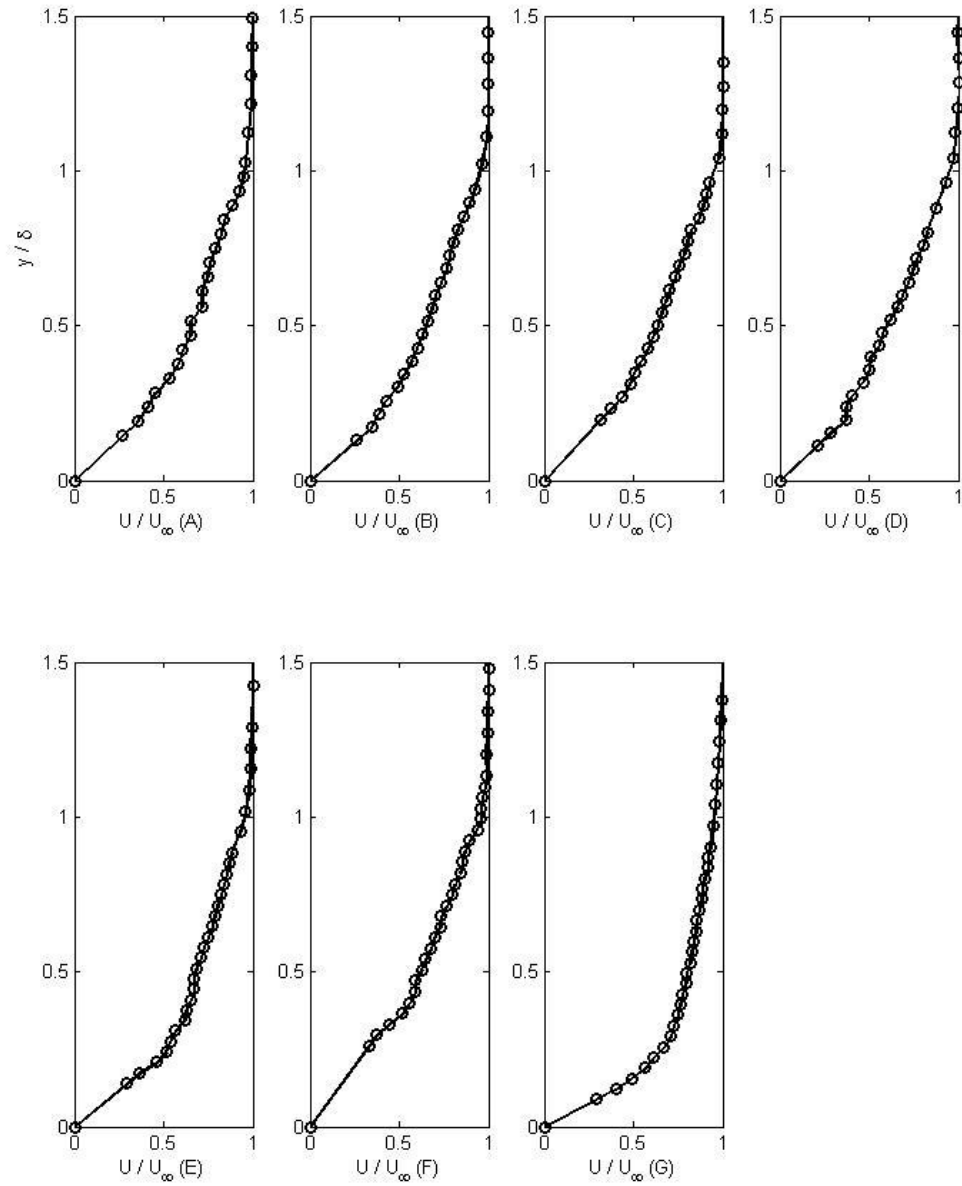


Figure 3.18 - Normalized boundary layer profiles, actuation frequency = 500 Hz, different streamwise locations (A) 7.5", (B) 8.0", (C) 8.5", (D) 9.0", (E) 9.5", (F) 10.0", and (G) 12.0"

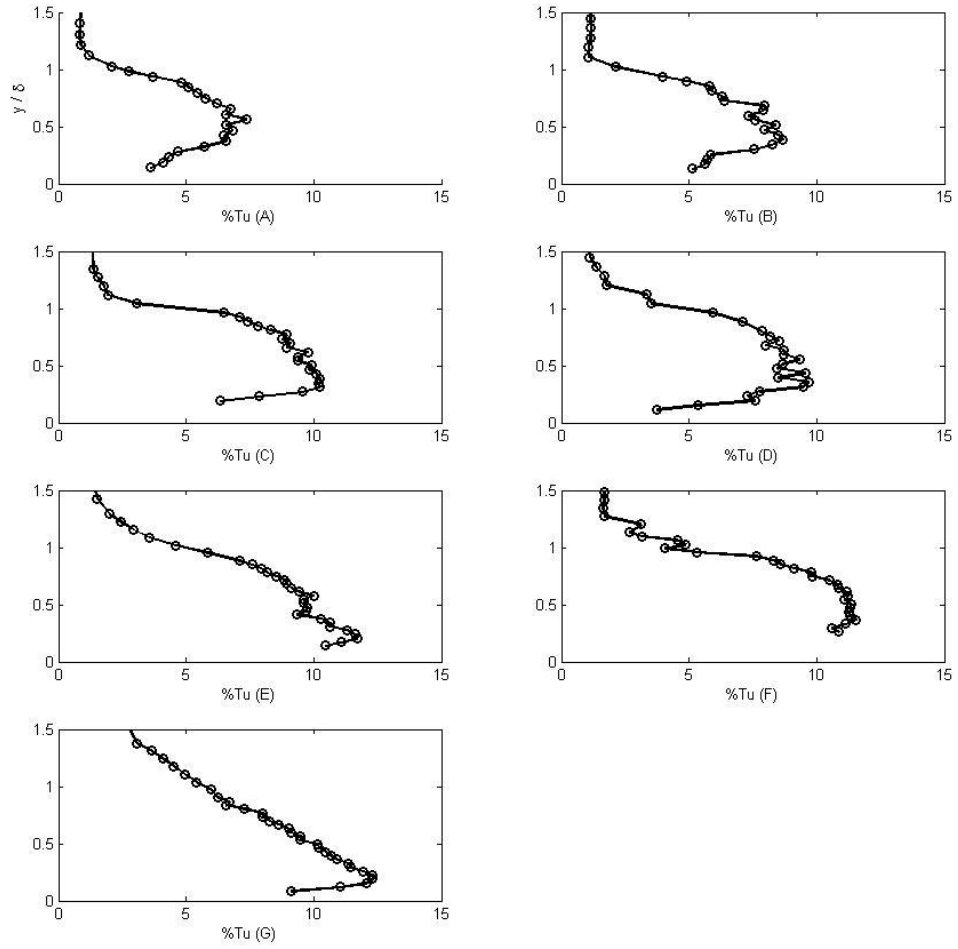


Figure 3.19 - Turbulence intensity profiles, actuation frequency = 500 Hz, different streamwise locations (A) 7.5", (B) 8.0", (C) 8.5", (D) 9.0", (E) 9.5", (F) 10.0", and (G) 12.0"

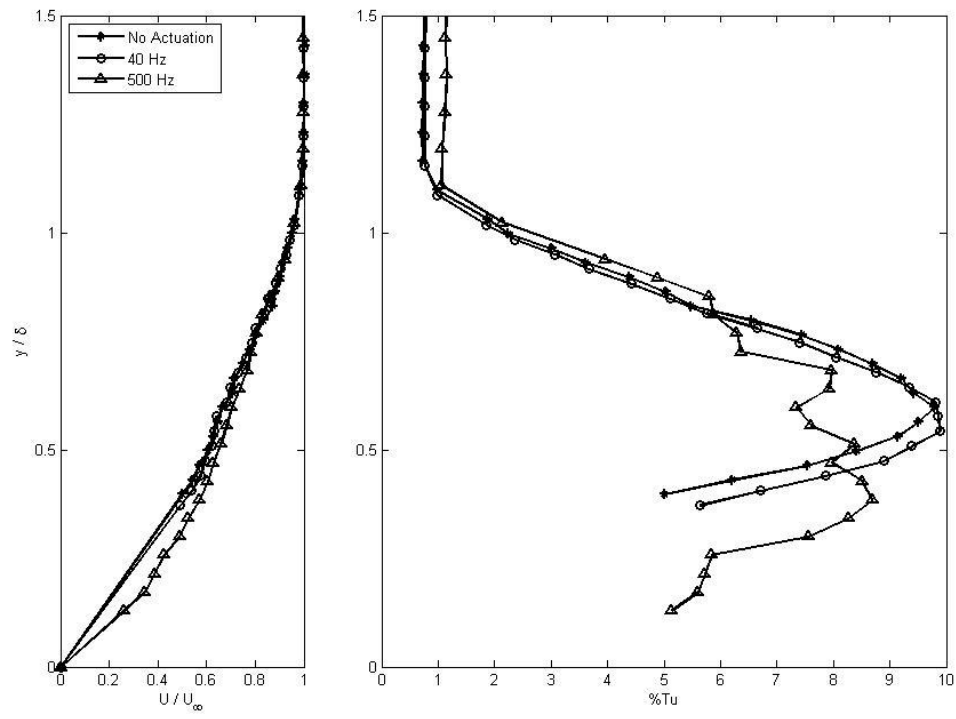


Figure 3.20 - Normalized boundary layer profile and turbulence intensity for different actuation frequencies, distance from leading edge = 8.0"

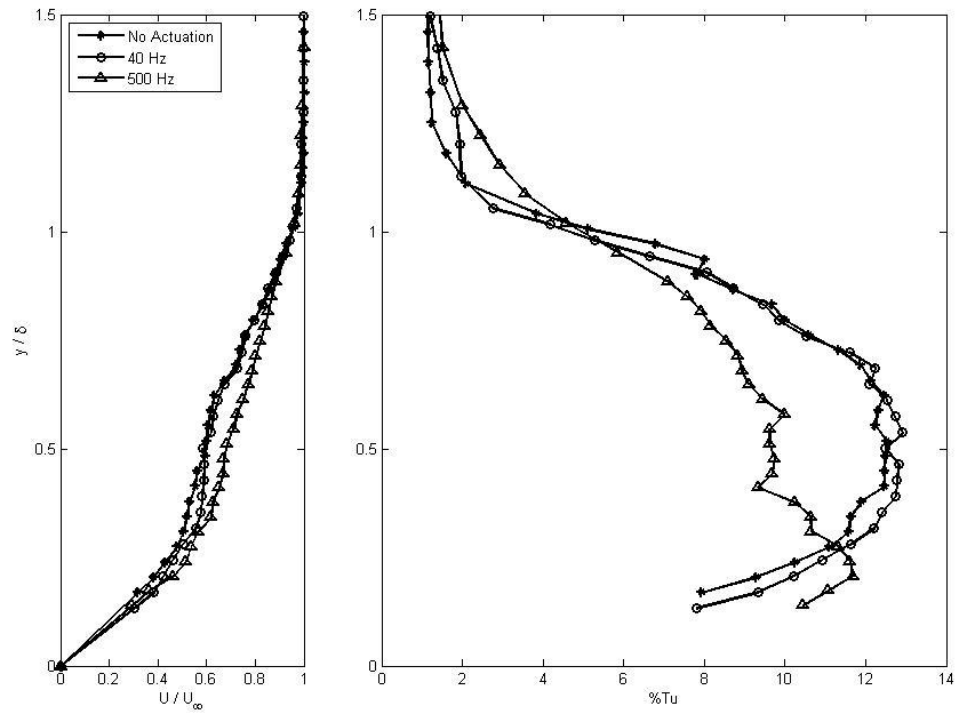


Figure 3.21 - Normalized boundary layer profile and turbulence intensity for different actuation frequencies, distance from leading edge = 9.5"

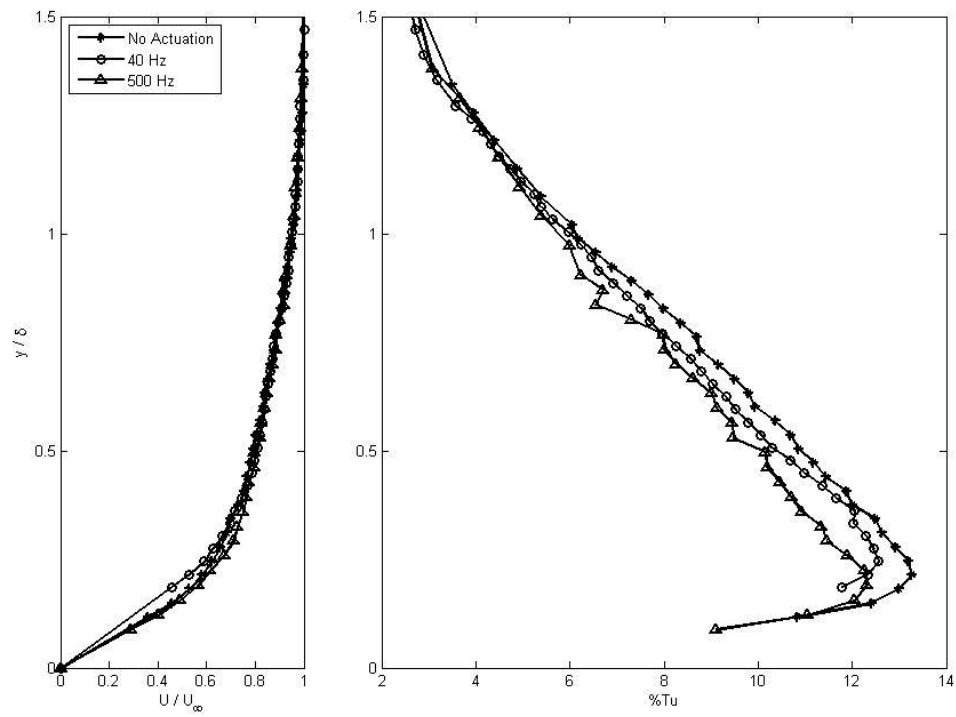


Figure 3.22 - Normalized boundary layer profile and turbulence intensity for different actuation frequencies, distance from leading edge = 12.0"

4. CONCLUSION

4.1 EAP Calibration

The response of an EAP to an input AC voltage with variable frequency was investigated experimentally using a Laser Displacement Velocimetry unit. Peak deflections were investigated for different voltages and frequencies across the surface of the polymer. Two different EAP units were tested: one under voltages of 1000V and 2000V with frequencies of 50Hz and 150Hz, the other under a voltage of 2000V with frequencies of 40Hz and 500Hz. The first EAP performed better at the higher frequency, reaching center displacements of up to 0.17mm. For the second EAP used in the experiments the lower frequency was more effective reaching a peak center displacement amplitude of 0.35mm at 40Hz and 0.25mm at 500Hz. The deflection profile against all the EAP units was parabolic.

4.2 Boundary Layer Measurements

An experimental investigation was conducted on the effects of an EAP on a flat plate boundary layer under an adverse pressure gradient. Boundary layer quantifications were completed using hot-wire measurements on the flat plate at trailing edge flap angles of 0 and 12 degrees. Boundary layer measurements were taken as a baseline for both flap angles to show the effect the flap has on the boundary layer, and it is clear that the flap induced an adverse pressure gradient. The flap caused a transitional region to occur at 7" to 10" downstream of the leading edge providing an area to test the EAP effectiveness on a sensitive boundary layer. Two frequencies were chosen for EAP actuation, 40Hz to excite the TS waves and 500Hz to excite the instabilities in the mixing layer. The higher frequency proved to be effective at smoothing the inflection point in the boundary layer as well as pulling the turbulence of the boundary layer closer to the surface of the plate. This indicates that the boundary layer is being made more stable and less susceptible to laminar separation. The frequencies corresponding to the TS waves were thought to be ineffective due to the state of the transitioning boundary layer.

It is clear that the EAPs were successful in altering a boundary layer with adverse pressure gradient and causing an early transition. This indicates that it could become a

useful flow control device, which can enhance the performance of MAVs; however, further experiments would be beneficial. At this stage, the main issues with EAPs as a flow control device are the necessary power to run them as well as the ruggedness of the actuator. As of now, in order to run the EAP a large amplifier is required, which definitely is not feasible for getting onto MAVs, especially more than one. A need for a small lightweight power source is required before the installment of the EAPs on an aircraft.

5. RECCOMENDATIONS FOR FUTURE WORK

Following this feasibility research it is clear that EAPs can be another big step in the field of flow control for low Reynolds number flight. There are a number of issues that need to be addressed in order for this actuator to be a viable option as a flow control device, such as robustness, surface smoothness, power requirements, and more.

The EAP used in the experiments at RPI was a single oscillating surface, but there are many more capabilities. Developing EAPs with surface dimples that can be individually activated will introduce yet another benefit to the flow control device, such as traveling wave and spatial distribution. Not only would the benefit from direct excitation of the flow would be there, but also different possibilities of streamwise and spanwise waves could be utilized, which would prove to be useful on three dimensional configurations, such as the MAVs. In addition, multiple small dimples could also add a roughness aspect (static or dynamic) to the flow control device, which is a well known and documented flow control technique. If properly utilized and explored, the EAP has countless possibilities in the field of flow control.

Bibliography

1. Abdullah, E., Bil, C. and Watkins S. 2009. Application of Smart Materials for Adaptive Airfoil Control. *AIAA paper* 2009-1359.
2. Amitay, M., Smith, D.R., Kibens, V., Parekh, D.E., and Glezer, A., Aerodynamic Flow Control over Unconventional Airfoil Using Synthetic Jet Actuators. *AIAA Journal*, **Vol. 39**, No. 3, 2001, pp. 503-529.
3. Bastedo, W.G. and Mueller, T.J., "Spanwise Variation of Laminar Separation Bubbles on Wings at Low Reynolds Number," *Journal of Aircraft*, Vol. 23, No. 9, 1986, pp.687-694.
4. Betchov, R. and Szewczyk, A. 1963. Stability of a shear layer between parallel streams. *Phys. of Fluids*, 6(10), 1391-1396.
5. Bruun, H. H., 1995. *Hot-Wire Anemometry*, Oxford University Press Inc., Oxford, New York.
6. Criminale, W.O., Jackson, T.L., and Joslin, R.D. 2003. *Theory and Computation in Hydrodynamic Stability*. Cambridge University Press. Cambridge, United Kingdom.
7. Dearing, S., Lambert, S., Morrison, J., 2007. Flow control with active dimples. *The Aeronautical Journal*. Paper No. 3174.
8. Diwan, S. and Ramesh, O. 2007. Laminar separation bubbles: Dynamics and control. *Sadhana*, **32**, 103-109.
9. Ehlers, S.M. and Weisshaar, T.A. 1993. Static Aeroelastic Control of an Adaptive Lifting Surface. *Journal of Aircraft*. Vol. 30, No. 4, July-Aug.
10. Gad-el-Hak, M. 2000. *Flow Control: Passive, Active, and Reactive Flow Management*. Cambridge University Press. Cambridge, United Kingdom.
11. Gaster, M. 1967. The Structure and Behaviour of Separation Bubbles. *Aeronautical Research Council Reports and Memoranda*, 3595.
12. Gaster, M. 1974. On the effects of boundary-layer growth on flow stability. *Journal of Fluid Mechanics*.**66**: 465-480.
13. Goksel, B. 2007. Plasma Flow Control at MAV Reynolds Numbers. *3rd US-European Competition and Workshop on Micro Air Vehicle Systems*.

14. Ifju, P.G., Jenkins D. A., Ettinger, S., Yongsheng, L., Shyy, W., and Waszak M.R., 2002. Flexible-Wing-Based Micro Air Vehicle. AIAA Paper 2002-0705.
15. Joslin, R.D. 1998. Aircraft Laminar Flow Control. *Annual Review of Fluid Mechanics*. Vol.30: 1-29.
16. Lang, M., Rist, U. and Wagner, S. 2004. Investigations on controlled transition development in a laminar separation bubble by means of LDA and PIV. *Experiments in Fluids*, **36**, 43-52.
17. Lessen, M. 1950. On stability of free laminar boundary layer between parallel streams. NACA Report 979.
18. Lock, R.C. 1951. The velocity distribution in the laminar boundary layer between parallel streams. *Quart. J. Mech. Appl. Math.*, 4, 42-62.
19. Marxen, O., Lang, M., Rist, U., and Wagner, S. 2003. A Combined Experimental/Numerical Study of Unsteady Phenomena in a Laminar Separation Bubble. *Flow, Turbulence and Combustion*, **71**,133-146.
20. Marxen, O., Kotapati, R.B., and You, D. 2006. Evaluation of active control of a laminar separation bubble based on linear stability theory. *Center for Turbulence Research Annual Research Briefs*. 323-335.
21. Mueller, T.J. and DeLaurier, J.D., 2003. Aerodynamics of Small Vehicles. *Annual Review of Fluid Mechanics*. **Vol. 35**, pp. 89-111.
22. Narasimha, R., and Prasad, S.N.1994. Leading edge shape for flat plate boundary layer studies. *Experiments in Fluids*. **Vol. . 17**, No. 5, pp. 358-360.
23. Pinkerton, J.L. and Moses, R. W. 1997. A Feasibility Study To Control Airfoil Shape Using THUNDER. *NASA Technical Memorandum*, **4767**.
24. Prandtl, L. 1904. Fluid Motion with Very Small Friction. *Proc. Third Int. Math. Mech.* **5**. pp. 484-491. Heidelberg, Germany.
25. Schlichting, H. 1932, Uber die Entstehung der Turbulenz bei der Plattenstromung. *Math. Phys. Klasse*, pp. 160-98.
26. Schlichting, H. 1979. *Boundary-Layer Theory*. 7th Ed. The Mcgraw-Hill Book Company, Inc.. Germany.
27. Thibert, J.J., Reneaux V., Schmitt, V. 1990. ON-ERA activities in drag reduction. *Congr. Int. Counc. Aeron. Sci.* 17th, pp 1053-64.

28. Tilly, A. and Sousa, J. 2008. Kelvin-Helmholtz Instability Due to Slot Blowing in Laminar Boundary Layers. *AIAA Journal*, **46**, No. 6.
29. Tollmien W. 1926. Über die Entsehung der Turbulenz. *Math. Phys. Klasse*, pp.21-44.
30. Udovitchik, N., Morrison, J.F., 2006. Investigation of Active Dimple Actuators for Separation Control. AIAA Paper 2006-3190.
31. White, F. M. 2006. *Viscous Fluid Flow*, Third Edition. McGraw-Hill Companies, Inc.. New York, NY.
32. Zhang, W., Hain, R., Kahler, C.J. 2007. Scanning PIV study on the laminar separation bubble on the SD 7003 airfoil. *7th International Symposium on Particle Image Velocimetry*.